KeAi
CHINESE ROOTS
GLOBAL IMPACT

Available online at www.keaipublishing.com/en/journals/journal-of-magnesium-and-alloys/

ScienceDirect

Journal of Magnesium and Alloys 13 (2025) 592–612

www.elsevier.com/locate/jma

Full Length Article

Flash-PEO of magnesium: Phosphate precursor driven functionalization

M.H. Guerra-Mutis, J.M. Vega*, M.I. Barrena, E. Matykina, R. Arrabal

Departamento de Ingeniería Química y de Materiales, Facultad de Ciencias Químicas, Universidad Complutense de Madrid, 28040, Spain

Received 22 October 2024; received in revised form 9 January 2025; accepted 13 January 2025
Available online 31 January 2025

Abstract

In this study, a phosphate-based conversion coating (PCC) was applied as a precursor before forming silicate-fluoride (SiF) and silicate-phosphate-fluoride (SiPF) based flash-plasma electrolytic oxidation (Flash-PEO) coatings on AZ31B magnesium alloy. The main novelty is the successful incorporation of calcium, zinc, manganese and phosphate species into the Flash-PEO coatings via a precursor layer rather than using the electrolyte. The precursor also led to longer lasting and more intense discharges during the PEO process, resulting in increased pore size. Corrosion studies revealed similar short-term performance for all coatings, with impedance modulus at low frequencies above 10^7 Ωcm^2, and slightly better performance for the SiPF-based coating. Nonetheless, the enlarged pores in the PEO coatings functionalized with the PCC precursor compromised the effectiveness of self-healing mechanisms by creating diffusion pathways for corrosive species, leading to earlier failure. These phenomena were effectively monitored by recording the open circuit potential during immersion in 0.5 wt.% NaCl solution. In summary, this study demonstrates that conversion coatings are a viable option for the functionalization of PEO coatings on magnesium alloys, as they allow for the incorporation of cationic and other species. However, it is crucial to maintain a small pore size to facilitate effective blockage through self-healing mechanisms.

Keywords: AZ31B magnesium alloy; Phosphates; Chemical conversion coating; Flash plasma electrolytic oxidation; Electrochemical impedance spectroscopy; Transmission electron microscopy.

1. Introduction

Surface modification of magnesium alloys has been a significant area of interest for both industry and academia since the mid-20th century, with a surge in research over the last three decades driven by their potential in lightweight applications [1,2]. The primary focus has been on enhancing the corrosion resistance of magnesium alloys to meet environmental regulations and specific demands of sectors such as transport, consumer goods, industry and biotechnology. Unlike aluminium, magnesium lacks the ability to form a stable, protective oxide layer when exposed to corrosive environments. Additionally, its high chemical activity, indicated by a low reduction potential (−2.37 V vs. SHE) [3], makes it particularly susceptible to galvanic corrosion in the presence of electrolytes [4].

To address these challenges, a variety of surface modification technologies have been investigated [2,5–10], including powder spraying [7], laser treatment [11], sol-gel processes [12], electrochemical methods [13], corrosion inhibitors [14,15], conversion coatings [16], PEO post-treatments [17,18] and hybrid coating systems [19]. Conversion coatings (CC) and plasma electrolytic oxidation (PEO) are among the most studied due to their ease of application and compatibility with additional protective layers such as paints. Both CC and PEO primarily result in magnesium oxide-based coatings, but the incorporation of specific bath chemistries, such as phosphate-based compounds, has been shown to yield corrosion resistance comparable to chromate treatments, while being more environmentally friendly [7].

Phosphate conversion coatings (PCC) on magnesium alloys are produced using acidic formulations containing phosphates, salts containing Ca, Sr, Zn and Mn and other additives such as inhibitors and accelerators [20]. The aim is to form insoluble phosphates, which provide some corrosion protection

* Corresponding author.
E-mail address: jevega@ucm.es (J.M. Vega).

https://doi.org/10.1016/j.jma.2025.01.007

and serve as a base layer with good adhesion for paints. PCC formation occurs through local increase in pH near the surface, which triggers the nucleation and growth of phosphates, accompanied by hydrogen evolution as a side reaction [21].

PEO processing of magnesium alloys provides diverse options for current regimes, including direct current, pulse unipolar, pulse bipolar and alternating modes [22]. It also allows for a wide range of voltage and current density values [23], among other parameters. PEO processing involves the use of alkaline electrolytes, typically containing silicates, phosphates, aluminates, fluorides or their combinations, along with high voltages to generate electric discharges that facilitate the formation of oxide compounds with incorporated electrolyte species. Phosphates in the electrolyte aid in the formation of phosphorus-containing coatings, predominantly in amorphous phases. These phosphates contribute to self-healing mechanisms by dissolving and reprecipitating at locations where the PEO coating deteriorates during service [24].

One of the main limitations of PEO processing is its relatively high energy consumption. There are several approaches to overcome this limitation, such as additives, electrolyte suspensions and Flash-PEO, which significantly shortens the process duration to under 100 s, resulting in thinner but still corrosion-resistant coatings [25]. Another strategy involves the use of precursor layers, as demonstrated by the authors for PEO of aluminium alloys [26]. An additional benefit of precursors is that the final 'structured' coating may outperform the stand-alone precursor layer and PEO coatings, as they incorporate functionalities from both systems (e.g. wear and corrosion protection). For example, different types of precursor layers have been used to obtain thick PEO coatings, such as laser shock peening [27], ultrasonic cold forging [28], cold spray [29–31] and preliminary PEO layers [32–34], among others. Moreover, the wide range of chemical formulations available for precursor layers offers flexibility in coating design. Therefore, the use of precursors could eventually eliminate the need for unstable additives in PEO electrolytes, simplifying electrolyte composition and reducing maintenance costs.

The use of conversion coatings as precursors in PEO treatment of magnesium alloys has been relatively unexplored [35–37]. Hariprasad et al. [35] applied a 15 min DC pulsed PEO process on AZ31 magnesium alloy preconditioned with a 4 h CeCC pretreatment. The resulting CeCC-PEO coating showed increased thickness, reduced surface porosity and enhanced corrosion resistance, along with favourable bioactivity in Kokubo simulated body fluid. Zhu et al. [36] demonstrated improved corrosion resistance of AZ91D magnesium alloy in 3.5 wt.% NaCl solution after using a molybdate conversion coating (MoCC), formed in a Na_2MoO_4–Na_3PO_4 bath at 60 °C for 40 min, followed by 30 min of DC PEO in a borate-silicate electrolyte. The MoCC precursor lowered the arcing voltage and promoted a more uniform coating with $MgAl_2O_4$ and $MoSi_2$ phases, reducing the corrosion current density. Qian et al. [37] combined a ~15 μm-thick ZnCC precursor, produced by immersing pure magnesium in an acidic Zn-P solution for 20 min, with an 11 min AC PEO treatment in silicate or phosphate electrolytes. The ZnCC-PEO coatings featured a Zn-rich outer layer, enhancing both thickness and chemical stability of the PEO system. Additionally, the PEO coating in the phosphate electrolyte demonstrated antibacterial effects when activated by ultrasonic vibration or ultraviolet irradiation, due to the release of reactive oxygen species. This coating also exhibited promising osteogenic and cytocompatibility properties. However, regardless of the precursor, all the examples mentioned above rely on extended PEO treatments (at least 10 min to produce thick PEO coatings) rather than shorter treatments (e.g. 60 s, which result in thin PEO coatings known as Flash-PEO).

The main novelty of the present work is the incorporation of elements such as Mn, Zn and Ca into the coating composition throughout the integration of a precursor layer (rather than using an electrolyte) into a thin Flash-PEO coating. The morphology and corrosion performance of these Flash-PEO coatings are studied on the AZ31B magnesium alloy using two different electrolytes: silicate-fluoride (SiF) and silicate-phosphate-fluoride (SiPF). Characterization is performed using X-Ray Diffraction (XRD), Scanning Electron Microscopy (SEM) coupled with an Energy-Dispersive X-Ray Spectroscopy (EDS) and Transmission Electron Microscopy (TEM). The corrosion performance of the coatings is assessed by means of Open Circuit Potential (OCP) measurements and Electrochemical Impedance Spectroscopy (EIS) during immersion in a 0.5 wt.% NaCl solution.

2. Materials and methods

2.1. Materials and electrolytes

The AZ31B alloy used in this study is composed on average by 3% Al (2.5% - 3.5%) and 1% Zn (0.6% - 1.4%), in balance with other elements considered as functional impurities: Si <0.08%, Cu <0.01%, Ni <0.001%, Mn 0.2% - 1.4%, Fe <0.005% and Ca <0.04%. The AZ31B magnesium alloy specimens were prepared to final dimensions of 40 mm in length, 30 mm in width and 3 mm in thickness, providing a total effective treatment area of approximately 2.9 cm^2. The edges of the samples were bevelled to minimize electrical charge accumulation associated with boundary effects during the PEO process.

The chemical solutions for the PCC and PEO electrolytes were prepared in deionized water with continuous stirring, as follows: a) phosphate conversion coating (PCC, pH 2.5): 1 L of solution containing 2 g/L ZnO, 12 g/L H_3PO_4, 4.74 g/L $C_4H_4O_6Na_2{\cdot}2H_2O$, 6 g/L $NaNO_3$, 0.5 g/L $Na_4P_2O_7$, 5.81 g/L $Ca(NO_3)_2{\cdot}4H_2O$ and 6.17 g/L $Mn(NO_3)_2{\cdot}4H_2O$ [20]; b) silicate based electrolyte (SiF, pH 12.8 ± 0.3, 25.4 ± 1.4 mS/cm): 2 L of solution containing 2.8 g/L KOH + 10 g/L $Na_2SiO_3{\cdot}5H_2O$ + 3 g/L KF [38]; and c) silicate and phosphate based electrolyte (SiPF, pH 12.6 ± 0.2, 24.1 ± 0.6 mS/cm): 2 L of solution containing 2.8 g/L KOH, 5 g/L $Na_2SiO_3{\cdot}5H_2O$, 5 g/L $Na_3PO_4{\cdot}12H_2O$ and 3 g/L KF [38].

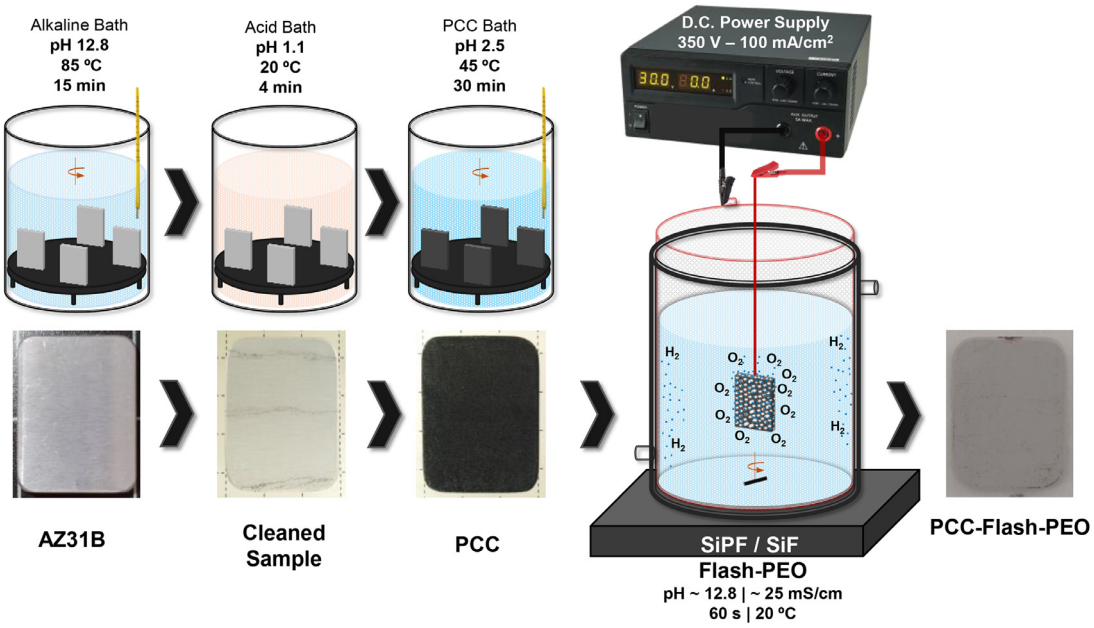

Fig. 1. Schematic representation of the full surface treatment process: cleaning, PCC and Flash-PEO.

2.2. Phosphate conversion coating

After mechanical preparation (P600 SiC paper), a two-step commercial pretreatment procedure (degreasing and pickling) was performed. The samples were mounted on a custom-built inert support to ensure controlled immersion into the different baths. The first pretreatment step involved immersion in an alkaline surfactant solution (Bonderite C-AK 4181 L; pH 12.8; 90 g/L), maintained under agitation for 15 min at 80–90 °C. This was followed by acid pickling (Bonderite C-IC 3610; pH 1.1; 10 g/L) for 4 min at room temperature. After rinsing with deionized water, the samples were dried up for 2 min in a stream of warm air. Finally, the samples underwent the conversion process for 30 min at 45 °C in the PCC acid bath, where a dark grey phosphorus-rich coating was formed, which turned light grey after drying with warm air. The final coating thickness was 19.1 ± 4.3 μm.

2.3. Flash plasma electrolytic oxidation

Flash-PEO was carried out using two different electrolytes [38]: i) SiF and ii) SiPF. The main difference between these electrolytes is the presence (SiPF) or absence (SiF) of sodium phosphate (Na_3PO_4). Four different systems are obtained: (1) SiF, (2) SiPF, (3) PCC-SiF, and (4) PCC-SiPF. These combinations are designed to explore the incorporation of phosphates either as a salt in the electrolyte (system 2) or as a precursor layer (systems 3 and 4), having system 1 as a reference "phosphate-free" coating.

Flash-PEO was conducted under continuous stirring in a double-walled glass reactor equipped with a water-cooling system, maintaining the electrolyte at 20 °C. A cylindrical grid made of 316 L stainless steel was used as the cathode, while the AZ31B alloy (w/o or with the PCC layer) served as the anode. The electrodes, positioned 67.5 mm apart, were connected to a DC power supply (Delta Elektronika, SM400-AR-8) via an insulated and threaded copper rod to ensure proper electrical contact. A constant current density of 100 mA/cm^2 and a voltage limit of 350 V were applied for a treatment time of 60 s [25], providing the proper conditions to facilitate a current drop between 30 and 40 s. After PEO treatment, the samples were rinsed with deionized water and sprayed with isopropanol, followed by drying with a stream of warm air. The thicknesses of the coatings without and with precursor were 5.3 ± 1.2 μm and 8.9 ± 2.4 μm, respectively. A schematic representation of the entire surface treatment process is shown in Fig. 1, which also summarizes the experimental conditions.

2.4. Characterization

The surface of the samples was inspected using optical microscopy (OM) with a Leica DMi8 M inverted microscope coupled to Leica Application Suite software. Roughness measurements were carried out with a focus variation optical profilometer (InfiniteFocusSL, Alicona GmbH) equipped with X10 and X50 lenses, using IFMeasure Suite software to extract roughness parameters S_a (arithmetical mean height of the area) and $S10_z$ (ten-point height). Water contact angle measurements were conducted with a FTA1000 B Class (First Ten Angstroms, Inc.) instrument equipped with a high-speed camera (Edmund Optics 5582) and a Navitar lens connected via the FTA32 interface. The drop volume was about 10.8 ± 0.6 μL and the height was around 3.0 mm (measured from the tip of the needle). The contact angle measurements were repeated in three different locations for each sample. Coating thicknesses were determined as the average of fifteen measurements using a Fischer ISOSCOPE-FMP10 portable eddy

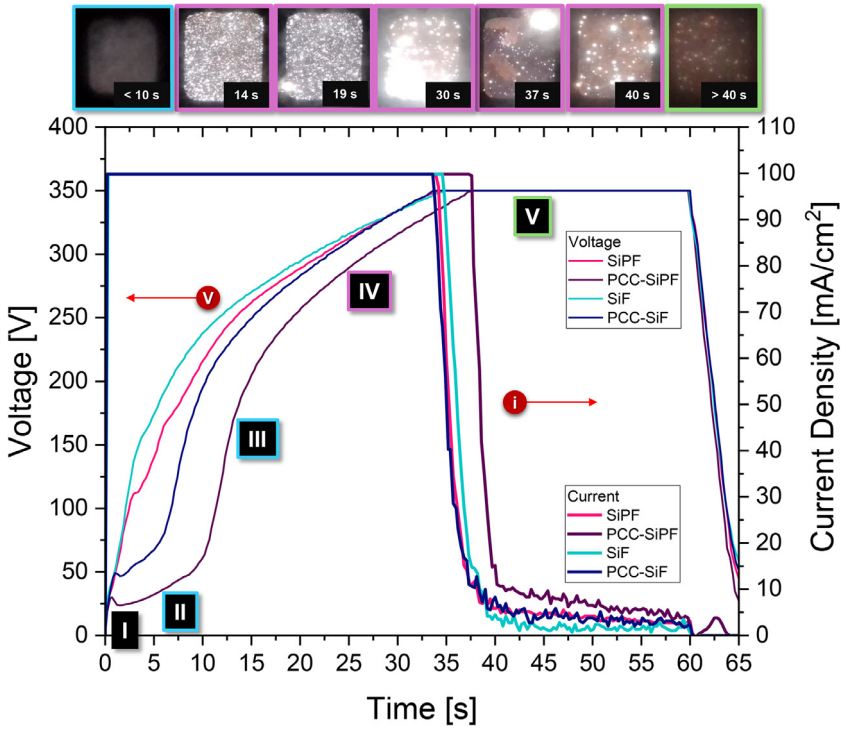

Fig. 2. Discharge evolution and correlation with the Voltage-Current vs. Time for SiF, SiPF, PCC-SiF and PCC-SiPF coatings. The inset images correspond to PCC-SiPF.

current meter and these results were further confirmed with cross-sectional SEM images.

Scanning electron microscopy (SEM) was performed using a Jeol JSM-6400 microscope, which was equipped with both X-ray Energy Dispersive Spectroscopy (EDS) and a Backscattered Electron (BSE) detector. Cross-sectional samples were embedded in epoxy resin and prepared by gradual griding using abrasive paper ranging from P120 to P4000, followed by polishing with 0.1 μm diamond paste.

Transmission electron microscopy (TEM) analysis was conducted with Jeol JEM 2100HT and Jeol JEM 3000F STEM microscopes, both equipped with X-ray energy EDS microanalysis systems and operating at accelerating voltages of 200 kV and 300 kV, respectively. Cross-sectional samples for TEM were prepared by gluing slices of the treated surfaces to create a sandwich approximately 1 mm^3 in size. These samples were mechanically ground to a thickness below 10 μm, fixed to a hollow disk of 2.5 mm in diameter and 80 μm thick, and then perforated using a 691 GATAN Precision Ion Polishing System (PIPS). Diffraction analysis was carried out using CrysTBox-Crystallographic Toolbox [39].

X-ray diffraction (XRD) measurements were carried out using a Panalytical X'Pert MRD X-ray diffractometer (Cu Kα =1,54,056 Å) at a grazing incidence angle of 0.5°. The scan range was 2θ from 10° to 90°, with a step size of 0.04° and a counting time of 15 s per step. The XRD spectra were analysed using the Panalytical Xpert High Score Plus software and the PDF5+ database.

In order to explore the evolution of the different coatings with time, continuous open circuit potential (OCP) measurements over a 7-day period were carried out in a 0.5 wt.% NaCl solution. Moreover, electrochemical impedance spectroscopy (EIS) measurements were conducted at least by triplicate, following the standard UNE-EN ISO 16,773–2:2017 [40], using an Autolab PGSTAT30 potentiostat controlled by NOVA 2.1.6 software (Metrohm). The working electrode area was set to 1 cm^2, with a silver/silver chloride electrode (Ag/AgCl in 3 M KCl) serving as the reference electrode and a graphite rod as the counter electrode. The measurements were performed over a frequency range from 300 kHz to 10 mHz (75 points in total) using a sinusoidal amplitude of 7.07 mV_{rms}. The EIS spectra were analysed using ZView software (Scribner, LLC). The EIS diagrams were collected every day, ranging from 24 h to 168 h.

3. Results and discussion

3.1. Evolution of voltage and current during flash-PEO

Fig. 2 shows the current-voltage responses during Flash-PEO treatment, both with and without the PCC precursor. Following Ohm's Law, under a constant current density (set to 100 mA/cm^2), the voltage increases as the oxide film thickens. However, once the voltage reaches the predefined limit of 350 V, after 35–40 s, the electrical response changes. At this point, the voltage remains constant at 350 V and the current gradually decays until the treatment ends at 60 s, followed by an additional 5 s ramp-down phase. Representative images at different periods of the PEO process are shown in the inset

images (PCC-SiPF system), in the upper part of the figure, showing the specific time of the plasma process.

The most notable differences between the studied specimens are observed in the first 40 s, during which several stages can be identified based on voltage response and discharge characteristics. In the initial second of treatment (Stage I), the voltage increases similarly for all specimens due to the formation of a passive film, primarily consisting of magnesium oxide/hydroxide and other species present in the electrolyte (e.g., Si and F) [41].

During Stage II, between 25 and 125 V, fluctuations in the voltage slope are mainly attributed to oxygen evolution. This reaction is strong enough to cause partial detachment of the precursor material through mechanical action, resulting in voltage plateaus for the PCC-SiF and PCC-SiPF specimens. For PCC-SiPF, the change in slope occurs at a lower voltage (25 V) and the plateau persists longer compared to PCC-SiF (50 V). Similarly, the addition of phosphate leads to a slower voltage increase during Stage II when comparing the specimens without a precursor layer. Therefore, despite the SiF and SiPF electrolytes having very similar pH and conductivity, the presence of phosphate in SiPF has a noticeable effect on the voltage response during the first seconds of treatment. This effect is likely due to the surfactant properties of phosphates and their impact on oxygen evolution. A reduced surface tension in the SiPF electrolyte would facilitate gas bubble formation, prevent coalescence and promote the detachment of both gas bubbles and precursor material, thereby enhancing wettability and improving contact between the electrolyte and the substrate. This, in turn, reduces both resistance and voltage in accordance with Ohm's Law.

Eventually, the specimens with the precursor regain the steep voltage slope at around 7 s for PCC-SiF and 12 s for PCC-SiPF (Stage III), reflecting the thickening of the inner barrier layer of the coating. Following this, all specimens show a faint glow or luminescence over the entire surface, with a noticeable change in voltage slope at 210 V marking the onset of visible discharges on the surface (Stage IV). These discharges evolve from small, short-lived events to more intense and long-lasting ones, particularly in the specimens with the precursor. Additionally, for the PCC-SiPF specimen, there is a period of several seconds during which large, wave-like discharges slowly move across the regions of the surface with lower resistance, especially along the perimeter due to the edge effect, leaving behind a trail of smaller discharges. This indicates that the addition of phosphate to the PEO electrolyte also influences the discharge characteristics. Given that SiF and SiPF have similar pH and conductivity, this behaviour is likely related to the surfactant effect of phosphates, which modifies the properties of gas bubbles and, consequently, the discharges, making them more localized. Furthermore, the incorporation of phosphates into the growing coating could also affect the discharge characteristics.

Despite the initial delay, the specimens with the precursor also reach the voltage limit around 35–40 s, due to their slightly higher voltage slope during Stage IV. This increased slope is associated with the remaining precursor material on the surface, which facilitates the coating growth and results in higher impedance. Otherwise, if similar slope had obtained, the entire precursor layer would have been removed. Therefore, it confirms that certain PCC layer is still present on the surface during stage IV which is in agreement with thicknesses of the coatings: 8.9 ± 2.4 μm for the PCC-treated specimens compared to 5.3 ± 1.2 μm for those without the precursor. In the final 20–30 s of treatment (Stage V), the decreasing current density led to a reduction in discharge intensity, with no significant differences observed between the specimens. The supplementary material for this work includes videos for the studied materials, which visually demonstrate the aforementioned stages (Videos SV1, SV2, SV3 and SV4).

Calculation of the specific energy consumption, as explained in [42], yielded average values of 0.5 and 0.3 $kWh{\cdot}m^{-2}{\cdot}\mu m^{-1}$ for the treatments without and with precursor, respectively. Given that the electrical responses are similar, the difference in energy consumption is attributed to the variation in coating thickness. These values are typical for Flash-PEO processes and are considerably lower than those found in conventional PEO [43].

Table 1
Composition (at.%) of the AZ31B magnesium alloy coated with PCC. EDS locations are labelled in Fig. 3b.

PCC	O	Mg	Al	P	Ca	Mn	Zn
S1-Outer layer	67.2	1.2	–	15.3	2.8	4.9	8.6
S2-Inner layer	70.8	25.5	3.1	–	–	0.1	0.5
S3-Substrate	4.8	92.3	2.3	–	–	0.2	0.4

3.2. Coatings characterization

3.2.1. SEM of the PCC layer

Fig. 3 shows the BSE plan-view and cross-sectional micrographs of the PCC-treated AZ31B magnesium alloy. Two well-defined regions of the coating are visible: i) a homogeneous but cracked inner layer, and ii) an upper layer primarily composed of dispersed particles. Elemental analysis, as presented in Table 1, indicates that the particulate material consists mainly of calcium, manganese and zinc phosphates, consistent with the composition of the PCC bath, while the inner layer is primarily composed of magnesium oxide.

It is worth noting that the particulate material is easily removed from the conversion coating when subjected to ultrasonic cleaning, leaving behind a uniform thin layer attached to the surface of the AZ31B magnesium alloy, with a thickness of 7.3 ± 1.9 μm. For the purposes of this study, ultrasonic cleaning was omitted to preserve the original thickness (19.0 ± 4.3 μm), along with the particulate matter, which is primarily composed of phosphates.

3.2.2. SEM of the flash-PEO coatings without and with PCC precursor

Fig. 4 and Fig. 5 show the longitudinal and cross-sectional SEM micrographs of the studied Flash-PEO coatings, respectively. The typical small and numerous pores resulting from

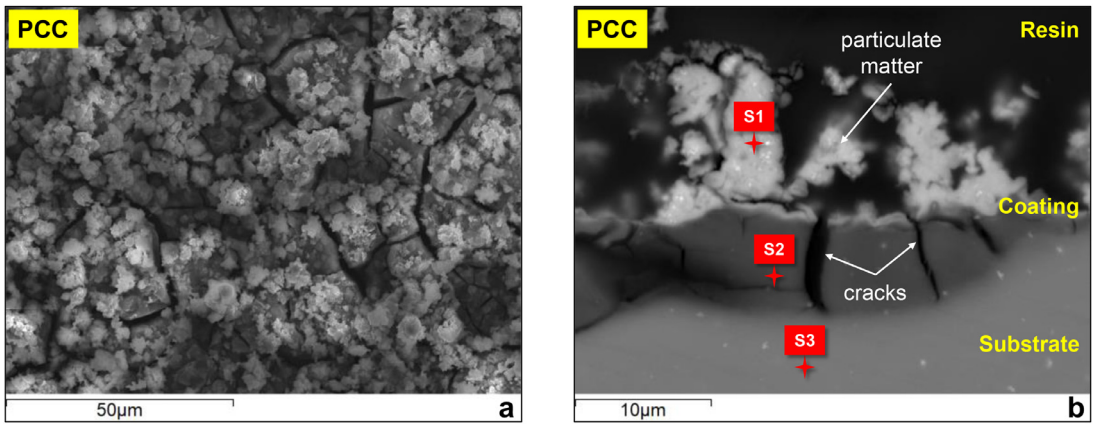

Fig. 3. BSE micrographs of AZ31B magnesium alloy with PCC: a) plan view; and b) cross section. EDS results are included in Table 1.

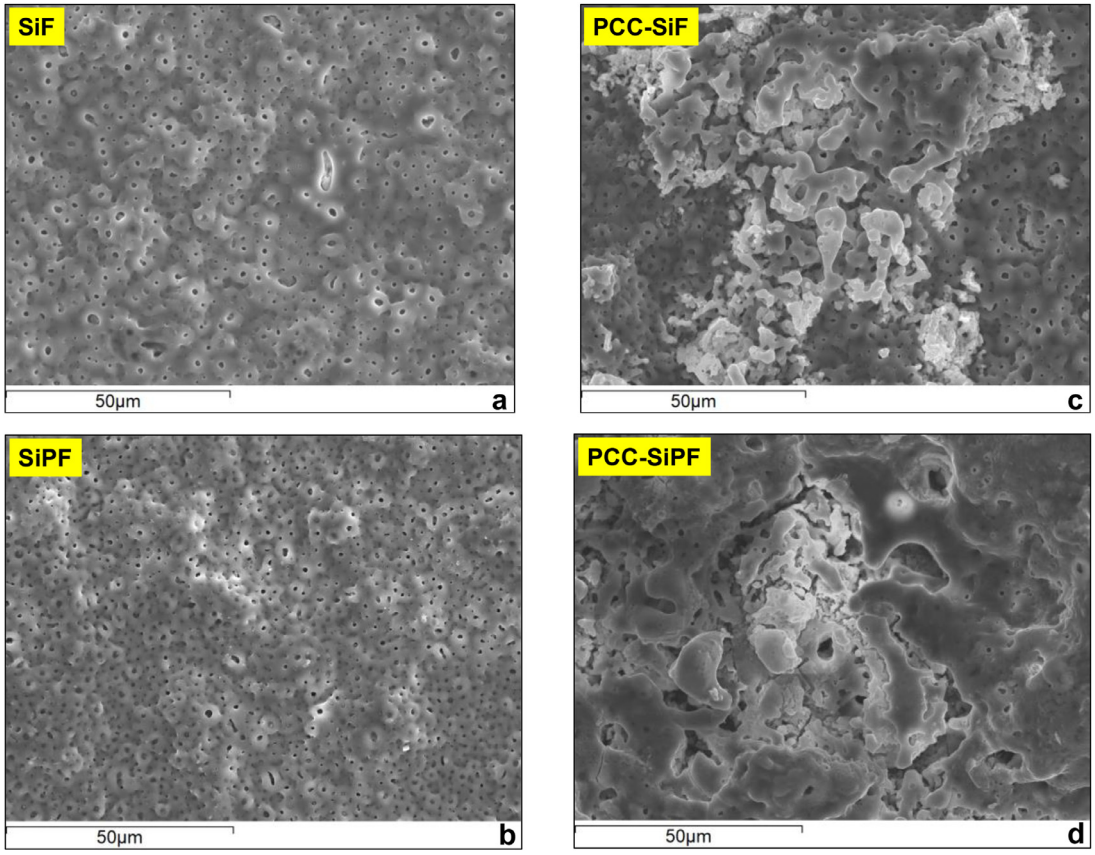

Fig. 4. Longitudinal SEM micrographs of: a) SiF, b) SiPF, c) PCC-SiF and d) PCC-SiPF.

Flash-PEO processing are evident in the specimens without the precursor layer (Fig. 4a and b). However, when the PCC layer is present, a completely different morphology is observed. There are regions with larger pores and a flake-like structure containing calcium, zinc, manganese and phosphorus from the PCC precursor (see EDS of the top layer in Table 2). The formation of larger pores is consistent with the longer-lasting and more intense discharges observed during Flash-PEO of PCC-treated specimens.

Although subtle, the material forming the flakes in the PCC-SiPF system appears more continuous than in the PCC-SiF one, leading to partial coverage of the surrounding areas and smaller pores (Fig. 4d). This smooth and continuous morphology is characteristic of PEO coatings produced in phosphate-based electrolytes and it may be partially attributed to the formation of P-rich amorphous phases [44,45].

The cross-sectional micrographs of SiF and SiPF specimens (Fig. 5a and b) reveal the formation of a relatively compact top layer, with vertical pores corresponding to the discharge channels. Beneath this top layer, an intermediate layer —often referred to as a ‘pore band’ [46] — contains smaller pores but also large ones at the base of the

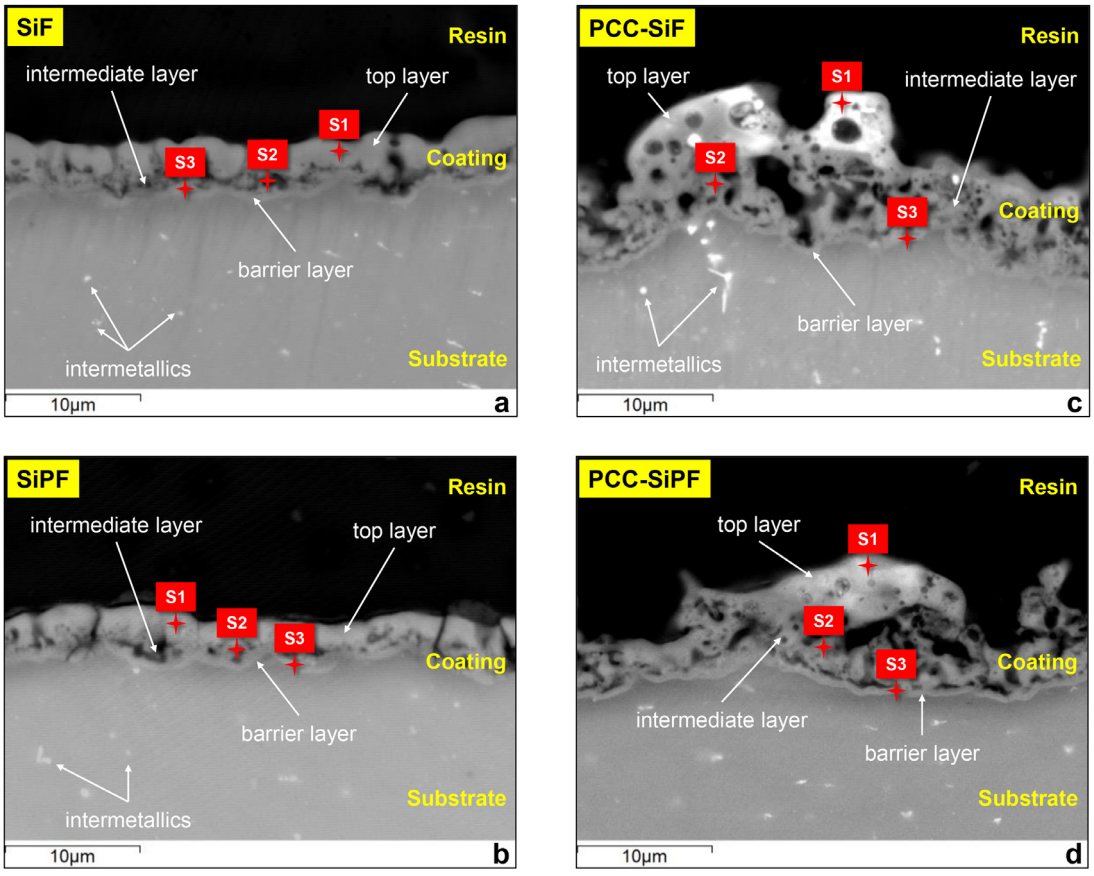

Fig. 5. BSE micrographs of the cross-sections of: a) SiF, b) SiPF, c) PCC-SiF and d) PCC-SiPF. EDS results are included in Table 2.

Table 2
EDS results (at.%) for the studied Flash-PEO coatings. EDS locations are labelled in Fig. 5.

	O	F	Mg	Al	Si	P	K	Ca	Mn	Zn
SiF										
S1-Top Layer	55.5	1.4	28.2	1.7	13.1	–	–	–	0.1	–
S2-Intermediate Layer	52.0	4.0	30.6	1.3	11.6	–	0.1	–	0.2	0.2
S3-Barrier Layer	31.8	12.4	49.6	2.0	3.7	–	–	–	0.2	0.3
PCC-SiF										
S1-Top Layer	58.2	–	12.3	4.2	6.7	5.6	1.7	1.4	4.4	5.5
S2-Intermediate Layer	48.3	9.1	32.8	2.4	6.7	0.2	0.2	–	0.1	0.2
S3-Barrier Layer	31.7	7.3	55.3	2.7	2.4	0.2	–	–	–	0.4
SiPF										
S1-Top Layer	56.8	4.1	28.5	1.9	5.9	2.7	–	–	0.1	–
S2-Intermediate Layer	46.3	7.4	36.7	1.5	4.3	3.3	0.2	–	0.1	0.2
S3-Barrier Layer	31.8	15.3	48.0	1.9	1.6	1.1	–	–	0.1	0.2
PCC-SiPF										
S1-Top Layer	61.1	–	17.5	2.5	1.8	10.3	1.6	0.7	1.6	2.7
S2-Intermediate Layer	51.0	7.8	32.8	2.7	3.3	1.9	0.2	–	–	0.2
S3-Barrier Layer	31.1	13.3	50.5	2.2	1.5	1.1	–	–	–	0.3

discharge channels. Finally, a dense inner barrier layer is present.

In contrast, when the PCC layer is used as a precursor, thicker coatings are obtained, and a less compact top layer is formed (Fig. 5c and d). This can be attributed to the longer-lasting, more energetic discharges that develop in thicker coatings [47]. It is important to note that these discharges partially destroy or detach the PCC precursor during Stage II of the current-voltage response (Fig. 2), which is confirmed by the reduction in thickness —from 19 µm in the PCC layer to 9 µm in the PCC-SiF and PCC-SiPF coatings.

EDS analyses performed on the top (S1), intermediate (S2) and inner (S3) layers reveal a consistent trend in the elemental distribution across all coatings: oxygen content increases from the bottom to the top of the coatings whilst magnesium and fluorine show the opposite trend, the latter being predominantly located into the barrier layer [48]. Higher concentra-

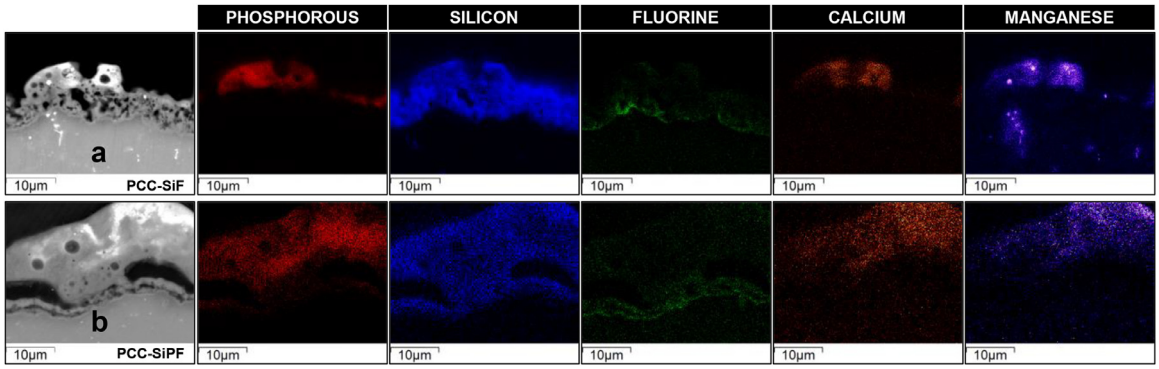

Fig. 6. EDS elemental maps of: a) PCC-SiF and b) PCC-SiPF coatings.

tions of silicon, phosphorus and elements originating from the PCC layer (i.e., Ca, Mn, Zn) are found in the top layer. Zinc and aluminium are also incorporated from the alloy substrate.

The most distinct feature of the PCC-SiF and PCC-SiPF coatings is the presence of isolated flakes that protrude above the regular coating thickness. EDS analyses reveal that these flakes are remnants of the PCC layer, transformed under the influence of the discharges. For example, the S1 spot (Fig. 5c) shows the presence of Mn, Zn and P (∼5 at.%) as well as K and Ca (∼1.5 at.%). This composition is similar to that of the particulate matter formed in the single PCC layer (Table 1), where Mn, Zn and P concentrations range between 5 and 15 at.%.

To provide a more detailed view of the distribution of elements originating from the PCC layer, Fig. 6 depicts the elemental maps for both structured coatings, PCC-SiF and PCC-SiPF. Fluorine and silicon show similar distributions in both systems: fluorine is mainly located within the barrier layer whilst silicon is dispersed throughout the entire coating. Manganese, calcium, zinc (not included) and phosphorus are concentrated in the upper part of both coatings, although phosphorus is more evenly distributed in the PCC-SiPF, since $(PO4)^{3-}$ is present in the SiPF electrolyte. These results confirm that phosphorus compounds are transferred from the PCC layer to the structured coatings, leading to phosphate-rich flakes, particularly evident in the PCC-SiF system. Another notable feature visible in the elemental maps is the oxidation of Al-Mn intermetallics into the PEO layer (Fig. 6a).

As previously mentioned, the discharges during Flash-PEO also cause partial detachment or destruction of the PCC pretreatment. To investigate this further, the PEO electrolytes were filtered after several specimen treatments and the solids were characterized using SEM-EDS. This analysis confirmed that some precursor material was detached during Flash-PEO (Figure S1 and Table S1). Additionally, the phosphate concentration in the SiF electrolyte was monitored after Flash-PEO processing of 5, 10, 12, 16, 20 and 26 PCC-treated samples. A UV–Vis spectrophotometer (Shimadzu ISR-2600i) was used in absorption mode, following a colorimetric method based on ASTM D515 (Figure S2). The results indicated a steady increase in phosphate concentration, although the overall concentration remained low, reaching only 35 ppm after 26 samples or ∼75 cm^2 of cumulative treated area.

Table 3
Pore diameter for the studied PEO coatings.

	SiF	SiPF	PCC-SiF	PCC-SiPF
D Max [µm]	5.7	5.9	16.7	13.7
D Avg [µm]	1.2 ± 0.5	1.0 ± 0.4	2.3 ± 1.5	1.1 ± 0.8
D Min [µm]	0.6	0.6	0.6	0.6
Porosity Average [%]	8.3 ± 1.9	7.8 ± 0.7	12.1 ± 1.7	7.3 ± 1.5

Finally, four plan-view SEM micrographs for each specimen at a magnification of x200 were analysed using the ImageJ software to determine the average, maximum and minimum pore diameters. The results (Table 3) indicate that while the minimum pore size is similar across all systems, the maximum pore size is significantly larger for the systems containing the precursor, especially in the PCC-SiF system, which reached a maximum pore size of 16.7 µm. When comparing the average pore size, it increases in the following order: SiPF < PCC-SiPF < SiF < PCC-SiF. Notably, the porosity area fraction is greatest for PCC-SiF (12.1 ± 1.7%), compared to the other systems, which range from 7.3 to 8.3%. Therefore, SiPF electrolyte provides a more homogenous pore size distribution and lower average porosity. Additional details on the pore size analysis can be found in the supplementary information (Figures S3, S4, S5 and S6).

3.2.3. TEM of the flash-PEO coatings without and with PCC precursor

Fig. 7a shows the cross-sectional TEM image of the SiPF coating, with approximately 5 µm of overall thickness. High magnification TEM reveals that the discharge channels are present in both the top and the barrier layer (Fig. 7b). Previous studies have identified these hemispheric regions of advancing coating growth (red circle in Fig. 7b) as indicators of melted and quenched material at the bottom of the discharge channels [49,50]. Supplementary Figure S7 shows additional micrographs and electron diffraction pattern of the SiPF system, revealing the amorphous/nanocrystalline nature of the coating.

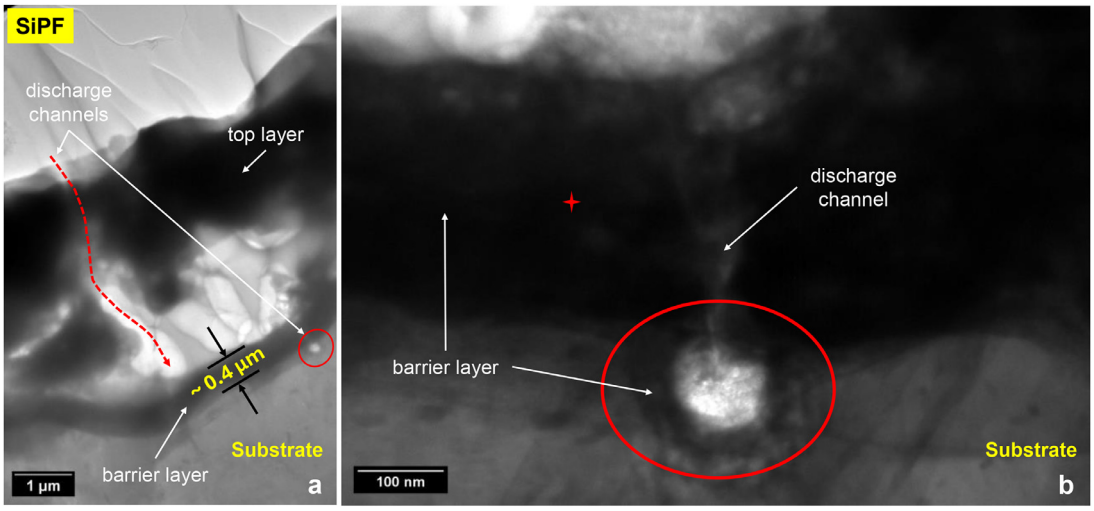

Fig. 7. a) Cross-sectional TEM micrograph of SiPF coating, and b) detail of the discharge channel in the barrier layer (@200 kV). The red cross in b) shows the location of the EDS analysis (Table 4).

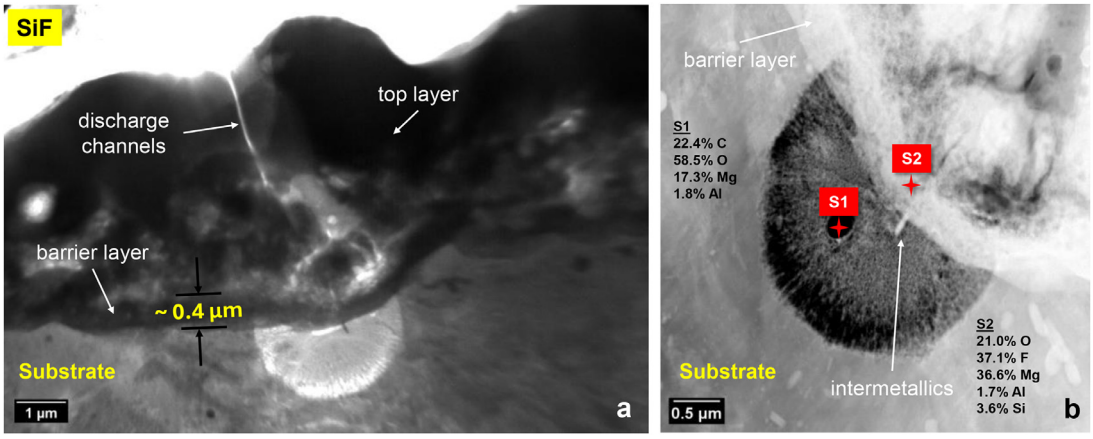

Fig. 8. TEM micrograph of SiF coating: a) General view @ 200 kV and b) Detail @ 300 kV. The damage caused by the EDS spot S1 is visible in b).

Table 4
Chemical composition (at.%) of the barrier layer shown in Fig. 7.

O	F	Mg	Al	Si	P	Mn	Zn
25.7	13.7	53.4	2.2	2.7	1.8	0.2	0.3

EDS analysis (Table 4) indicates that the barrier layer is composed of magnesium, oxygen and fluorine with smaller amounts of silicon and phosphorus. This 0.4 µm-thick barrier layer forms at the early stages of the oxidation process and is rebuilt after discharge events. Unlike in AC PEO processes, this barrier layer does not exhibit stratification [25].

TEM characterization of the SiF coating also revealed localized thickening of the oxide film at discharge channel locations, along with hemispherical regions featuring radial patterns (Fig. 8a). These regions result from the high energy input of the discharges, heating up the substrate beneath the barrier layer.

Fig. 8b highlights the 2.5 µm-diameter hemispherical region or 'disk' beneath the barrier layer, which is predominantly composed of magnesium oxide (see numbers in Fig. 8b). Given that the electrolyte is the only source of oxygen, the plasma channel carries a flow of oxygen ions [51] that effectively interact with the magnesium in the substrate.

Fig. 9 displays the EDS elemental maps corresponding to the micrograph shown in Fig. 8b. The oxygen map distinctly shows the disk of oxidized material located just beneath the barrier layer, produced by the discharge channel. Some carbon contamination is also observed, likely originating from the resin used during TEM sample preparation, but no traces of other electrolyte species, such as Si, P and F, are detected. These findings suggest that the hemispherical oxidized regions are the 'signature' of short-lived discharges that lack the time and energy to melt the surrounding coating at the substrate/coating interface but were sufficiently energetic within the plasma channel to melt and oxidize the substrate material directly impacted. The absence of significant amounts of Si, P and F indicates a rapid cooling period following the discharge event, which prevented the incorporation of these elements.

The EDS maps in Fig. 9 also reveal the presence of relatively unaffected Al-Mn(Fe) intermetallics within the oxidized

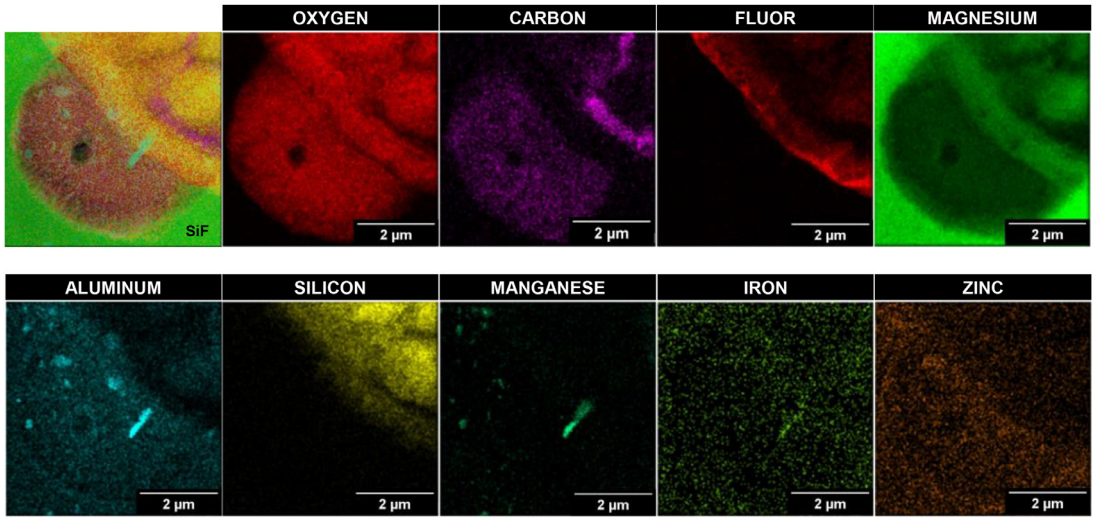

Fig. 9. STEM EDS maps of the micrograph shown in Fig. 8b.

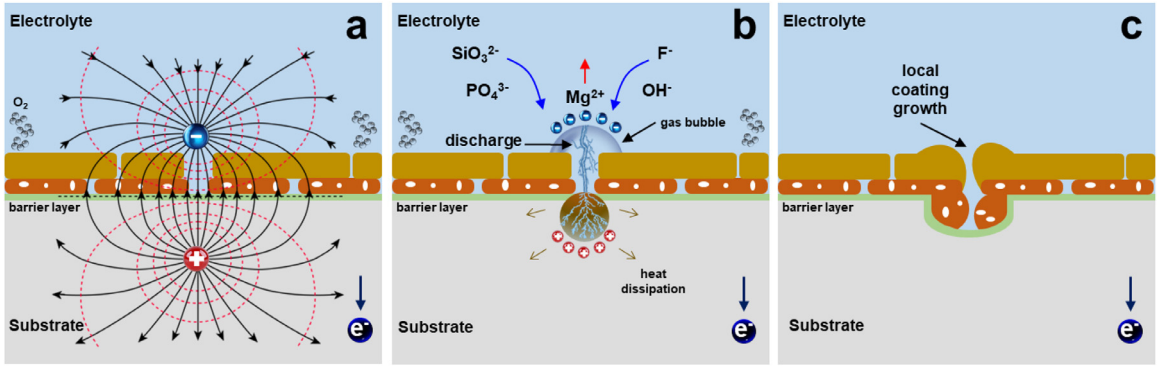

Fig. 10. Proposed sequence for the formation of the oxidized hemispherical regions: a) before breakdown, b) during breakdown, c) after breakdown.

'disk', confirming the limited energy supply associated with this discharge channel, as aluminium, manganese and iron are more difficult to oxidize compared to magnesium. Notably, the coincidence of the discharge channel with the location of intermetallics suggests that these compounds may play a role in initiating the discharges [52].

Fig. 10 schematizes a plausible sequence for the localized coating growth associated with localized discharges and gas bubble evolution, highlighting the formation of the hemispherical regions in the substrate, as described above. Fig. 10a depicts the first stage before dielectric breakdown, where the electric field strength increases at specific regions due to factors such as electrode configuration, surface irregularities and gas evolution [53]. At the same time, oxidation of the magnesium substrate and the electrolyte (i.e., oxygen evolution) occurs, similar to conventional anodizing processes.

In the second stage (Fig. 10b), as the electric field increases, intense polarization leads to dielectric breakdown across the barrier layer [47,51,54] or within gas bubbles or pores [55], along with the characteristic acoustic and light emissions of the discharge or plasma channel. It is believed that the bubble-electrolyte-substrate interface is a likely region for breakdown due concentration of the electric field lines. Under the influence of the electric field, electrons and reactive species such as H^+, OH^- and O^{2-} [56] are accelerated and react with the substrate and electrolyte species. The extreme temperatures in the discharge channel lead to electrolyte vaporization and localized melting and evaporation of the substrate in the shape of a small disk or hemispherical region. Notably, the radial features or Lichtenberg patterns [57] observed within the 'disk' shown in Fig. 8b resemble the early formation stages of positive streamers [58], commonly seen in water for pin-to-plate electrode configuration.

It has been proposed that expansion of the gas bubble, due to oxygen evolution, heat flow and vaporization of water increases the overall resistance in the plasma channel and, eventually, the current shuts down abruptly. The discharge event can be followed by a cascade of discharges at the same location, where the coating is acting as a dynamic capacitor, or can be followed by extinction if breakdown initiates elsewhere on the surface due to charge redistribution. In the latter case, plasma collapse is followed by bubble shrinkage and oxide condensation [51]. The second stage in Fig. 10b corresponds to the observed features in Fig. 8b and Fig. 9. However, the oxidized disks beneath the barrier layer are rarely reported in PEO studies, with the coating

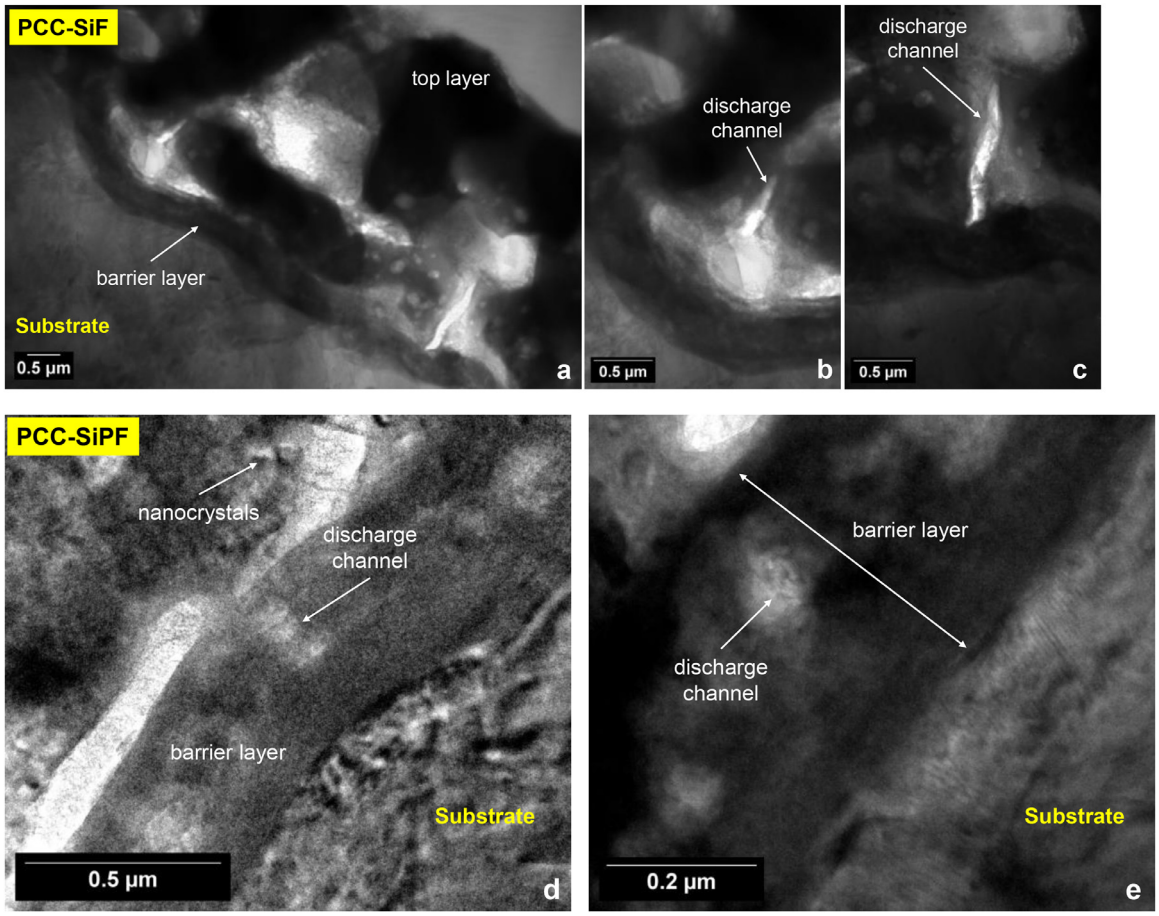

Fig. 11. Cross-section TEM images @ 200 kV for: a), b) and c) PCC-SiF, d) and e) PCC-SiPF.

morphology illustrated in the third stage (c) being far more prevalent.

When the plasma channel carries sufficient energy, its behaviour resembles arc welding process on a microscopic scale [59]. The sustained energy from the discharge causes both melting and evaporation of the substrate which quickly oxidizes. The molten material, present during and after the discharge, is influenced by various forces, such as electric fields, thermal buoyancy and Marangoni forces (i.e. thermocapillary effect). Marangoni forces dominate the shaping of the molten pool in welds [60]. However, the PEO process is more complex. High local pressures at the discharge sites drive the molten coating material into surrounding cavities or ejected it, creating the distinctive volcanic craters on the surface. The final result is localized thickening, with new oxide material accumulating at both the coating/electrolyte and coating/substrate interfaces, and a reconstructed barrier layer that extends further into the substrate, marking the location of the discharge events.

Fig. 11 shows the cross-sectional TEM micrographs of PCC-SiF and PCC-SiPF coatings, revealing similar morphologies characterized by discharge channels in both the porous and barrier layers, as well as localized coating growth. Although oxidized 'disks' were not observed in these systems, their presence remains plausible, as indicated by the remnants of discharge channels within the barrier layer.

3.2.4. X-ray diffraction

The XRD spectra for the PEO specimens are shown in Fig. 12, including the diffraction patterns of the AZ31B substrate and PCC as references. Regardless of the presence of a precursor layer (i.e., PCC), magnesium oxide is the predominant crystalline structure in all PEO coatings (Fig. 12a to 12 d). As for the phosphates, they can be assumed to be present as amorphous phases, with only the PCC system displaying a broad diffraction band at 22° 2θ. The absence of diffraction peaks associated with Si-rich phases indicates their amorphous nature, which can be attributed to the short process duration (60 s) and the moderate intensity of the discharges, which limit the energy delivered to the surface. Bragg-Brentano XRD analysis (not included here) further confirmed the absence of crystalline Si-rich compounds. In the systems containing the precursor (PCC-SiPF and PCC-SiF), the absence of this band suggests the transformation of the precursor layer although partial detachment or thinning cannot be ruled out.

3.2.5. Roughness and contact angle

Both S_a and S_{10z} roughness values were similar for the bare substrate and the SiPF and SiF systems (Table 5). This suggests that the Flash-PEO coating growth does not significantly alter the surface irregularities produced by the chemical etching pretreatment, even though these irregularities are

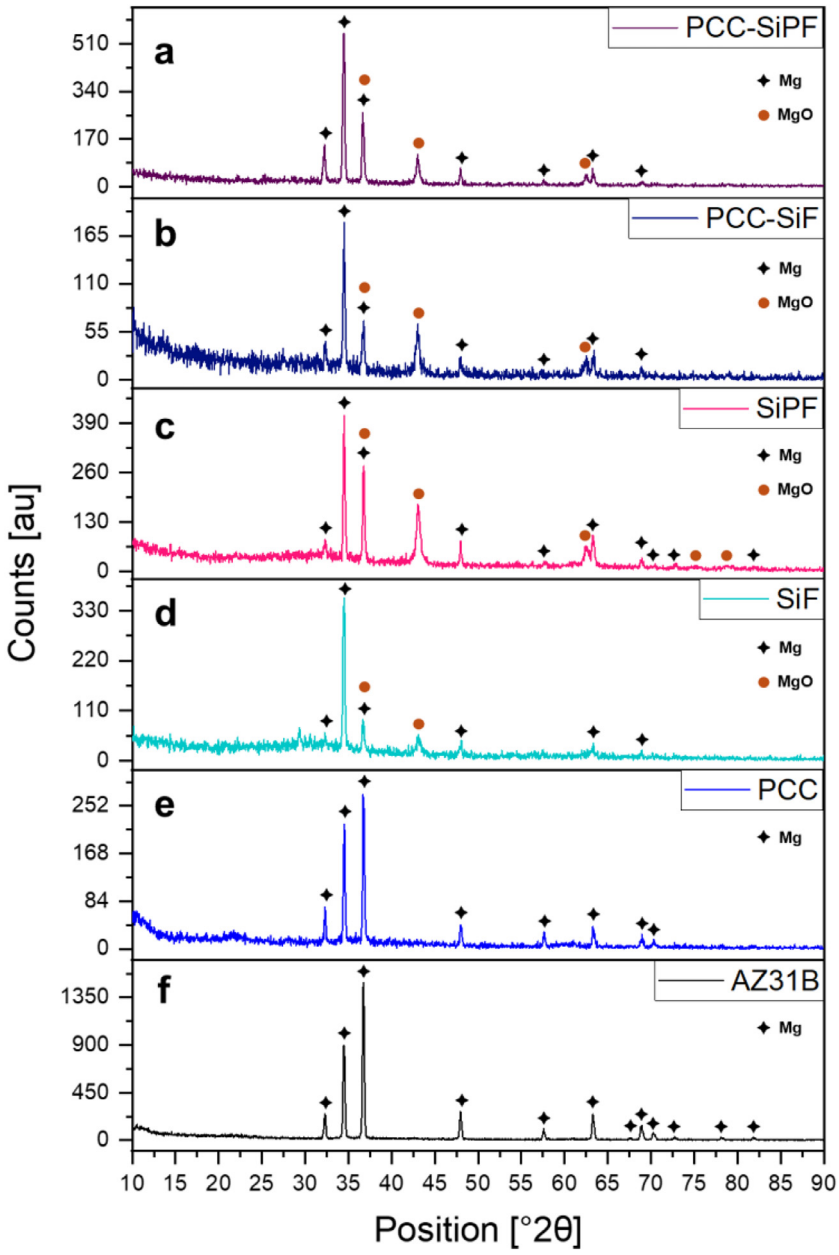

Fig. 12. XRD spectra for: a) PCC-SiPF, b) PCC-SiF, c) SiPF, d) SiF, e) PCC, and f) AZ31B.

favourable locations for discharge events, as noted by Nashrah et al. [53]. In contrast, the roughness of the PCC layer is much higher than that of the bare AZ31B (5.8 μm vs. 1.7 μm), leading to rougher surfaces in the PEO systems with a precursor layer (PCC-SiF and PCC-SiPF, 2.5 – 2.9 μm). This observation aligns with the distinct morphology shown in Fig. 4, where P-rich flakes decorate the surface of these structured systems.

According to ASTM STD D7334 − 08 (2022) [61], a surface is defined as hydrophilic when the contact angle is less than 45° and hydrophobic when is greater than 90°. Therefore, all systems can be considered hydrophilic except the etched AZ31B (Table 6). Additionally, a contact angle of 0° indicates perfect wetting (i.e., PCC and PCC-SiPF systems), while a contact angle greater than 0° but less than 90° indicates high wettability (i.e., SiPF, SiF and PCC-SiF) [62]. The perfect wetting (0°) observed in the PCC system is explained by the presence of a cracked layer, whereas in the PCC-SiPF system, the wettability may be attributed to the pore band (Fig. 5d and the surface morphology Fig. 4d) rather than roughness (Table 5) or pore size (Table 3). This could also explain the difference in wettability between the two precursor-containing systems (0° for PCC-SiPF vs. 20.6° for PCC SiF). Furthermore, the pore-size distribution (i.e., the cumulative relationship between fractional pore volume and finite pore size ranges) may play a key role [63]. If pores are physically connected, water can flow until it reaches a non-connected site, following a percolation phenomenon—

Table 5
Surface morphology and roughness of the studied systems.

Sample	Plan View [1 mm^2]	Sa[a] [μm]	S10z[b] [μm]
PCC-SiPF	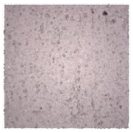	2.5 ± 0.1	35.4 ± 2.5
PCC-SiF		2.9 ± 0.1	33.6 ± 1.7
SiPF		1.5 ± 0.2	21.4 ± 1.0
SiF		1.6 ± 0.0	21.0 ± 2.5
PCC	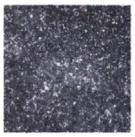	5.8 ± 0.1	68.3 ± 4.5
AZ31B		1.7 ± 0.1	19.2 ± 0.1

[a] Average height of selected area.
[b] Ten-point height of selected area.

Table 6
Contact Angle results for the studied coatings.

Sample	Contact Angle [°]
PCC-SiPF	0
PCC-SiF	20.6 ± 0.4
SiPF	28.5 ± 0.4
SiF	33.2 ± 0.3
PCC	0
AZ31B	99.0 ± 0.5

downward liquid movement through the pores or spaces in the material. In any case, the precursor-based coatings show improved wettability, which can be considered advantageous for applications involving water-based primers.

3.3. Corrosion evaluation

3.3.1. Open circuit potential

Fig. 13 shows the variation of the Open Circuit Potential (OCP) over time for six different systems. The AZ31B magnesium alloy, whether bare or coated with the PCC layer, shows a steady state value around −1.5 V, confirming that the PCC layer provides no significant protection, mainly due to the presence of cracks. In contrast, the four systems treated

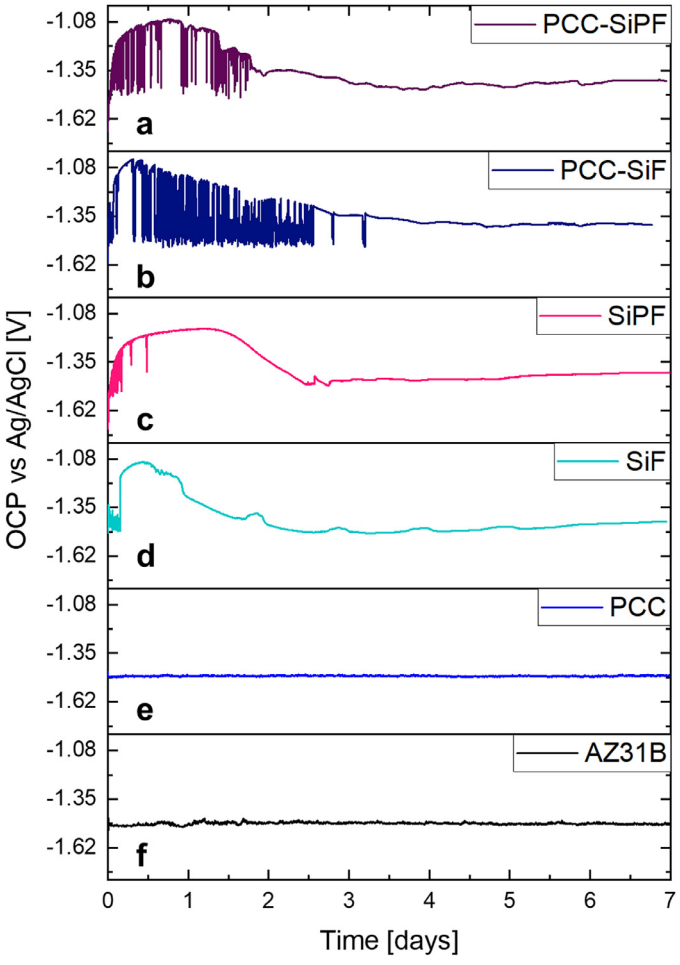

Fig. 13. Open Circuit Potential (OCP) for: a) PCC-SiPF, b) PCC-SiF, c) SiPF, d) SiF, e) PCC, and f) AZ31B.

with Flash-PEO show a similar trend over time: the OCP increases rapidly, reaching a maximum within the first 12 h of immersion and remains stable for approximately 24 h (stage I). This behaviour seems to be anomalous compared with the typical steady state values of the OCP in literature for sealed PEO coatings [64], indicating certain improvement of the corrosion protection with time. Interestingly, the SiF and PCC-SiF systems achieve the highest OCP values (between −0.9 V and −1.0 V), while the SiPF and PCC-SiPF systems reach a mixed potential of around −1.2 V. In stage II, all Flash-PEO systems experience a gradual decrease in potential, followed by a plateau after 3–4 days. Finally, in stage III, all systems converge to a similar potential after 7 days of immersion (around −1.4 V).

The two systems without precursor (SiPF and SiF) exhibit abrupt potential noise or metastable behaviour within the first 12 – 24 h of immersion, suggesting the activation and deactivation of localized corrosion processes (e.g. in defective zones of the barrier layer similar to those observed in Figs. 7b and 8). This metastable behaviour disappears after 24 h.

In contrast, the systems with a precursor (PCC-SiPF and PCC-SiF) show a prolonged metastable behaviour, with the

OCP fluctuating sharply. This indicates greater instability of the PEO layer, likely due to a combination of factors such as a higher number of defective zones in the barrier layer and increased electrolyte absorption (due to the presence of larger pores). However, this metastability disappears after 2 days in the PCC-SiPF system and after 3 days in the PCC-SiF system, which can be attributed to the self-healing effect of phosphates incorporated from the PEO electrolyte.

3.3.2. Electrochemical impedance spectroscopy (EIS)

Fig. 14 shows the average impedance modulus at low frequency, $|Z|_{0.01\ Hz}$, obtained from the Bode plot (log |Z| vs. log Frequency) for the different systems. Due to the dispersion of $|Z|_{0.01\ Hz}$ in systems with an inductive loop, the first |Z| value at which a plateau is reached in the Bode plot (usually between 10° and 10^1 Hz) was selected. This value was also validated with the diameter of the semicircle at low frequency—prior to the inductive loop—in the Nyquist plot.

The results indicate that the PCC system provides a $|Z|_{0.01\ Hz}$ of approximately 5×10^3 Ωcm^2 after 24 h of immersion, with values of 10^3–10^4 Ωcm^2 thereafter, which are very similar to those of the bare magnesium alloy, indicating negligible corrosion protection. In contrast, the PEO systems exhibit $|Z|_{0.01\ Hz}$ values above 10^7 Ωcm^2 after 24 h, followed by a progressive decrease over time, except for the PCC-SiF system, which shows an abrupt drop in impedance at 96 h. Although the impedance partially recovers at 120 h (to 5×10^4 Ωcm^2), it sharply declines again to values typical of bare AZ31B after 144 h and beyond. Slightly better behaviour is observed for the PCC-SiPF system, with $|Z|_{0.01\ Hz}$ reaching 5×10^5 Ωcm^2 after 96 h and remaining stable thereafter.

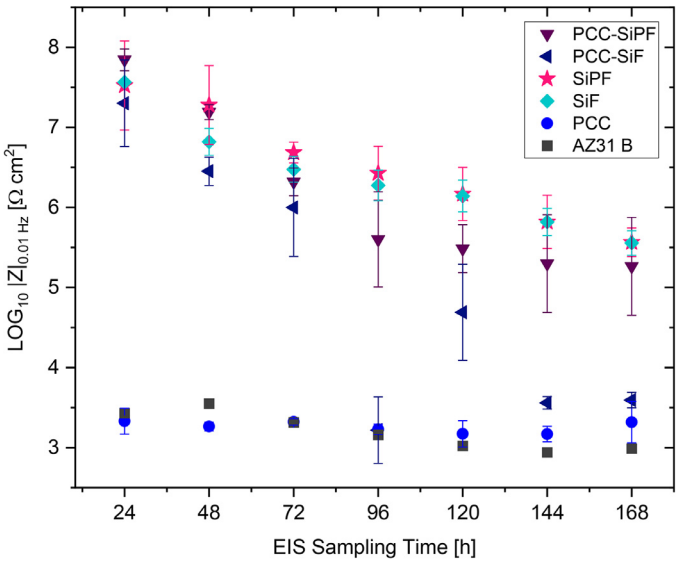

Fig. 14. Impedances recorded at 0.01 Hz (Bode plot) for all the systems in 0.5 wt.% NaCl solution.

The best performance is seen in the SiPF and SiF systems, which maintain values around 10^6 Ωcm^2 after 168 h.

Further analysis of the impedance results was conducted based on the shapes of the different impedance diagrams (e.g., Nyquist and the two Bode plots) after immersion times representative of the various stages reflected in the OCP evolution: (I) after 24 h, when the OCP value is at its maximum (Fig. 15); (II) after 96 h, once the OCP has completely decreased (Fig. 16); and (III) when the OCP stabilizes at 168 h (Fig. 17).

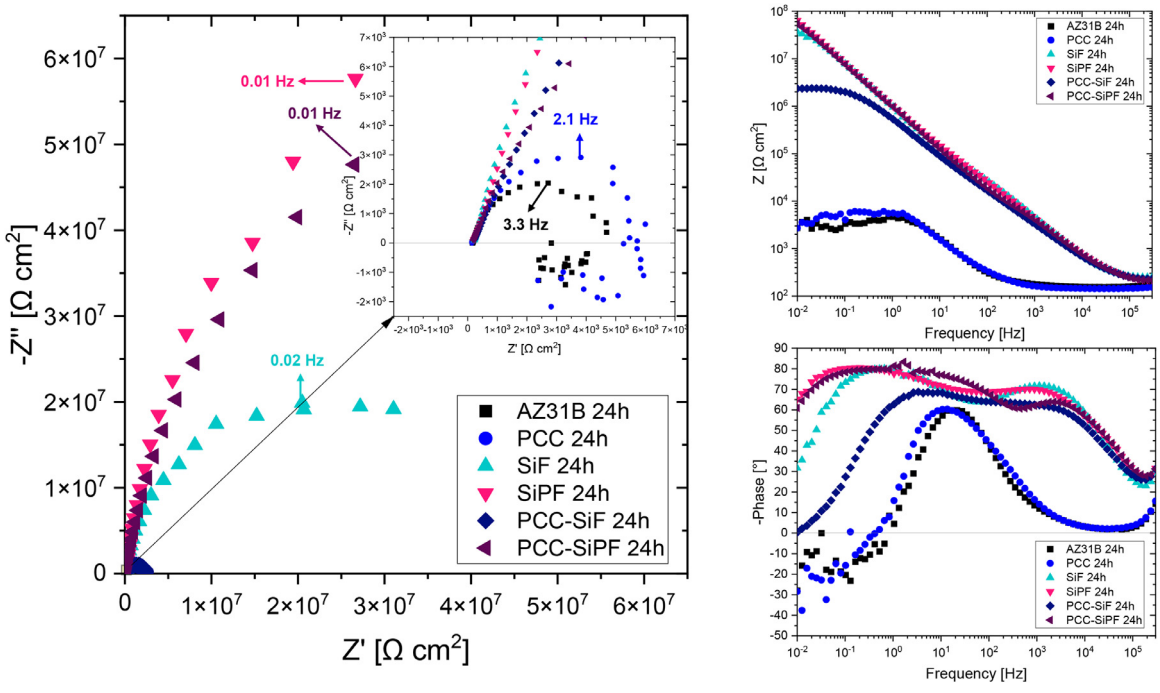

Fig. 15. EIS data after 24 h immersion. Comparison of the reference samples and coated samples.

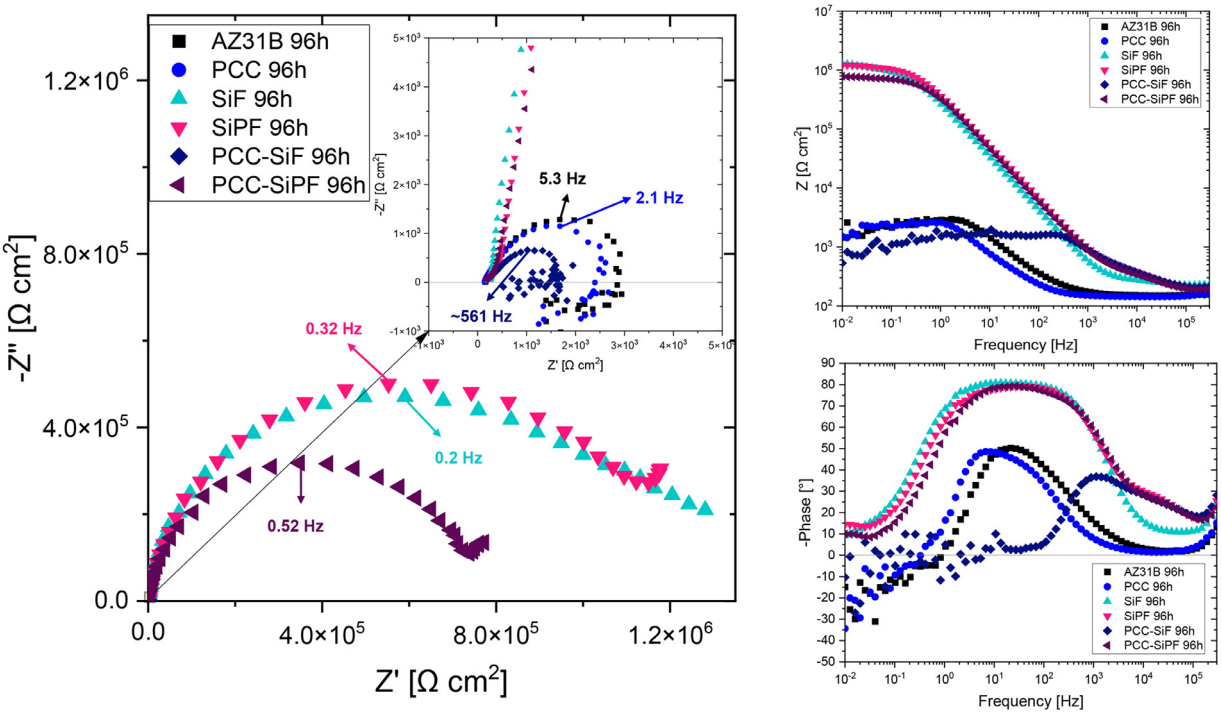

Fig. 16. EIS data after 96 h immersion. Comparison of the reference samples and coated samples.

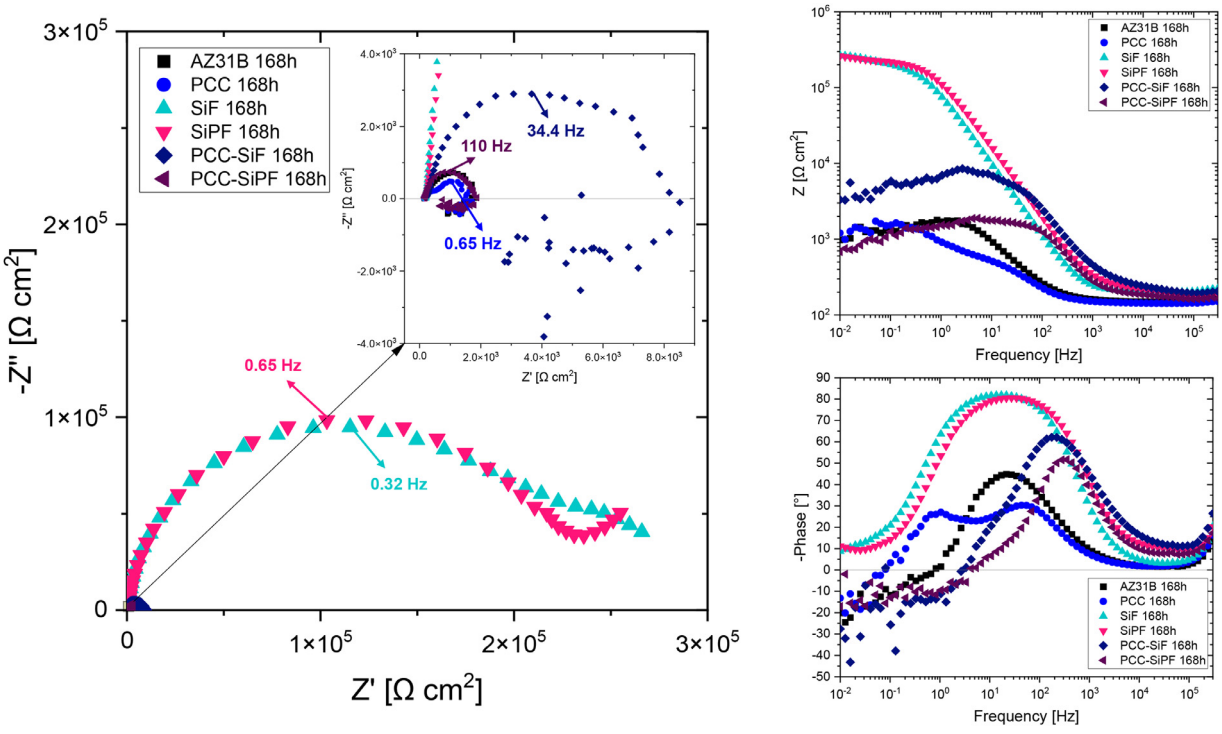

Fig. 17. EIS data after 168 h immersion. Comparison of the reference samples and coated samples.

As expected from the OCP results, the magnesium alloy covered by a PCC layer shows a similar impedance diagram to that of the bare AZ31B after 24 h of immersion (Fig. 15). A semicircle at high-to-medium frequencies and an inductive loop at low frequencies can be observed in the inset of the Nyquist plot, which is typical during the corrosion process of magnesium alloys [65]. In contrast, completely different diagrams are obtained for the PEO coatings, where two time constants are clearly evident in the Bode plot of phase angle vs. log frequency.

Equivalent circuits (EQ) were employed to gather more information about the performance of the coatings and reference

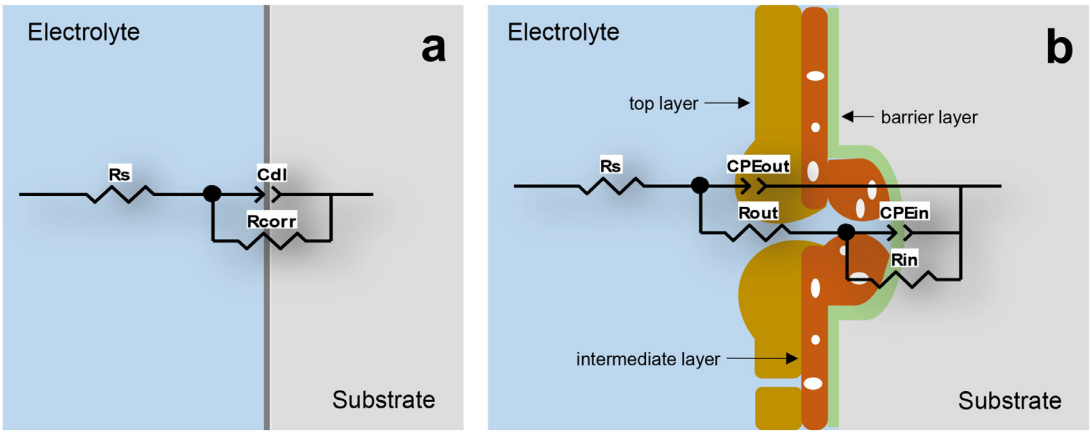

Fig. 18. Equivalent circuits for: a) AZ31B magnesium alloy and PCC up to 96 h immersion and b) PEO and PCC-PEO coatings (and PCC 168 h immersion).

Table 7
EIS parameters after immersion to 0.5 wt.% NaCl obtained by fitting the impedance diagrams using equivalent circuits with one or two time constants.

System	CPE_{PCC} ($\Omega^{-1}cm^{-2}s^{\alpha}$)	α_{PCC}	R_{PCC} (Ωcm^2)	CPE_{dl} ($\Omega^{-1}cm^{-2}s^{\alpha}$)	α_{dl}	R_{ct} (Ωcm^2)
AZ31B 24h				1.55×10^{-5}	0.87	4.98×10^{3}
AZ31B 96h				2.30×10^{-5}	0.78	3.64×10^{3}
AZ31B 168h				3.23×10^{-5}	0.80	1.90×10^{3}
PCC 24h				2.22×10^{-5}	0.80	9.38×10^{3}
PCC 96h				5.41×10^{-5}	0.76	3.61×10^{3}
PCC 168h	4.81×10^{-5}	0.79	5.66×10^{2}	2.98×10^{-4}	0.94	8.81×10^{2}
System	CPE_{out} ($\Omega^{-1}cm^{-2}s^{\alpha}$)	α_{out}	R_{out} (Ωcm^2)	CPE_{in} ($\Omega^{-1}cm^{-2}s^{\alpha}$)	α_{in}	R_{in} (Ωcm^2)
SiF 24h	1.13×10^{-7}	0.87	9.6×10^{4}	7.45×10^{-8}	0.96	4.82×10^{7}
SiF 96h	2.86×10^{-7}	0.83	1.16×10^{2}	3.79×10^{-7}	0.95	1.13×10^{6}
SiF 168h	1.97×10^{-6}	0.95	1.92×10^{5}	3.08×10^{-5}	0.64	1.21×10^{5}
SiPF 24h	1.28×10^{-7}	0.86	1.28×10^{5}	5.36×10^{-8}	0.94	3.30×10^{8}
SiPF 96h	2.43×10^{-7}	0.84	4.57×10^{2}	2.35×10^{-7}	0.94	1.20×10^{6}
SiPF 168h	5.24×10^{-7}	0.84	9.99×10^{1}	8.15×10^{-7}	0.96	2.27×10^{5}
PCC-SiF 24h	2.84×10^{-7}	0.79	3.94×10^{4}	3.68×10^{-7}	0.82	2.55×10^{6}
PCC-SiF 96h	2.62×10^{-5}	0.45	5.34×10^{2}	8.18×10^{-7}	0.83	1.72×10^{3}
PCC-SiF 168h	3.05×10^{-5}	0.53	1.66×10^{2}	1.22×10^{-6}	0.89	7.14×10^{3}
PCC-SiPF 24h	3.14×10^{-7}	0.76	1.58×10^{4}	1.95×10^{-7}	0.88	1.95×10^{8}
PCC-SiPF 96h	2.61×10^{-5}	0.46	3.01×10^{2}	5.07×10^{-7}	0.90	7.58×10^{5}
PCC-SiPF 168h	1.33×10^{-5}	0.57	8.05×10^{1}	1.34×10^{-6}	0.95	1.58×10^{3}

systems. Fig. 18 shows two scenarios where the inductive loop, if present, is neglected for simplicity: (a) a single time constant related to the corrosion process itself [65], characterized by the electrolyte resistance (Rs), the charge transfer resistance (R_{ct}) and the double layer capacitance (C_{dl}); and (b) a two-time constant scenario, where the time constant at high frequency may be associated with the porous outer layer ($\tau_{out} = R_{out} \times C_{out}$), and the one at low frequency with the inner barrier layer ($\tau_{in} = R_{in} \times C_{in}$) [66,67]. Moreover, in absence of pure capacitive behaviour, a constant phase element (CPE) can be used instead of capacitance: $CPE = Y_0^{-1}(j\omega)^{-\alpha}$. Here, Y_0 is the frequency-independent constant, $j^2 = (-1)$, $\omega = 2\pi f$ is the angular frequency in rad s^{-1}, f is the frequency in Hz, and the dimensionless α ($0 < \alpha < 1$) is related to the width of the distribution of relaxation times [68], where a value of 0.5 can be attributed to diffusion phenomena and values close to 1.0 indicate pure capacitance. Supplementary information from Figures S8 to S13 shows the fitting results at 24, 96 and 168 h of immersion for the six different systems.

The different impedance parameters are summarized in Table 7. Fitting results confirm that both bare AZ31B and PCC systems underwent corrosion processes [69]. Their single time constant (neglecting the inductive loop) exhibits CPE values of 10^{-5} $\Omega^{-1}cm^{-2}s^{\alpha}$, typical of double layer capacitance not only at 24 h but also after 196 h. A similar trend is observed for resistance values, which remain low ($R_{ct} < 10^5$ Ωcm^2). In contrast, the Flas-PEO systems exhibit two time constants that evolve with time as described below.

After 24 h (Fig. 15), and in agreement with the noble OCP values, the capacitance and resistance values indicate an almost complete lack of corrosion, as the high-frequency time constant shows a much lower CPE (10^{-7} $\Omega^{-1}cm^{-2}s^{\alpha}$) for all Flash-PEO systems compared to CPE_{dl}. This can be assigned

to the porous (top + intermediate) layer (CPE_{out}) while the low-frequency time constant corresponds to the barrier layer (CPE_{in}), showing the lowest values for the SiF and SiPF systems (10^{-8} $\Omega^{-1}cm^{-2}s^{\alpha}$). Notably, the precursor-containing systems display larger CPE_{in} values (10^{-7} $\Omega^{-1}cm^{-2}s^{\alpha}$), similar to CPE_{out} values, suggesting that the barrier layer is more protective in systems without a precursor (SiF and SiPF). The porous layer resistance (R_{out}) is comparable to R_{ct} ($< 10^5$ Ωcm^2) primarily due to the presence of pores, while R_{in} exceeds two orders of magnitude larger than R_{out} ($R_{in} > 10^7$ Ωcm^2).

After 96 h (Fig. 16), the Nyquist plot indicates that the PCC-SiF system is no longer protective, displaying an inductive loop absent in the other three PEO systems. This failure can be facilitated by the highest porosity average (12.1 ± 1.7%) compared to the other coatings. This aligns with the significant parameters changes shown in Table 7: a large increase in CPE_{out} (2.62×10^{-5} $\Omega^{-1}cm^{-2}s^{\alpha}$), with an α_{out} value of 0.45 indicating diffusion phenomena, alongside drastic decreases in R_{out} (5.34×10^2 Ωcm^2) and R_{in} (1.72×10^3 Ωcm^2). The PCC-SiPF system presents similar figures to PCC-SiF for the porous layer ($CPE_{out} = 2.6 \times 10^{-5}$ $\Omega^{-1}cm^{-2}s^{\alpha}$, $\alpha_{out} = 0.46$ and $R_{out} = 3.01 \times 10^2$ Ωcm^2), but retains a high R_{in} (7.58×10^5 Ωcm^2), slightly lower than the outstanding systems without precursors (both R_{in} and $|Z|_{0.01\ Hz}$ around 10^6 Ωcm^2). SiF and SiPF also show signs of barrier layer degradation at 96 h, as confirmed by the decrease in R_{in} and the increase in CPE_{in} (from approximately 10^{-8} $\Omega^{-1}cm^{-2}s^{\alpha}$ at 24 h to 2–4 $\times 10^{-7}$ $\Omega^{-1}cm^{-2}s^{\alpha}$ at 96 h). The primary difference between SiF and SiPF appears in the Bode diagram shape (phase angle vs. log frequency) at high frequency, likely linked to pore blockage influenced by their varying pore size distributions (i.e. self-healing mechanisms are more likely to occur in the smaller pores of the SiPF system, Table 3).

After increasing the immersion time to 168 h (Fig. 17), the Nyquist plot reveals the failure of the PCC-SiPF system, evidenced by an inductive loop. This is corroborated by the low $|Z|_{0.01\ Hz}$ ($< 10^4$ Ωcm^2) compared to SiF and SiPF systems, which present $|Z|_{0.01\ Hz}$ an order of magnitude larger ($> 10^5$ Ωcm^2). Despite a decrease in R_{in} from 10^6 Ωcm^2 (96 h) to 10^5 Ωcm^2 (168 h), SiF and SiPF continue to offer corrosion protection compared to the PCC precursor systems. Furthermore, significant differences arise between SiF and SiPF: i) a notable increase in R_{out} (three orders of magnitude) at 168 h vs. 96 h (1.92×10^5 Ωcm^2 vs. 1.16×10^2 Ωcm^2) for SiF, likely linked to pore blockage which confirms the self-healing behaviour linked to sealing effects, ii) the Nyquist plot reveals a third unresolved time constant at low frequency (previously observed at 96 h, Fig. 16): manifested as a new semicircle for SiPF system, contrasting with an overlapped time constant for the SiF system (flattened or depressed semicircle at low frequencies); iii) SiPF maintains the lowest CPE values ($CPE_{out} = 5.24 \times 10^{-7}$ $\Omega^{-1}cm^{-2}s^{\alpha}$ and $CPE_{in} = 8.15 \times 10^{-7}$ $\Omega^{-1}cm^{-2}s^{\alpha}$) compared to SiF ($CPE_{out} = 1.97 \times 10^{-6}$ $\Omega^{-1}cm^{-2}s^{\alpha}$ and $CPE_{in} = 3.08 \times 10^{-5}$ $\Omega^{-1}cm^{-2}s^{\alpha}$), with CPE_{in} for SiF exhibiting a typical value for double layer capacitance (C_{dl}); and iv) the α_{in} parameter is closer to 0.5 than 1.0 (0.64), indicating some degradation of the barrier layer, likely linked to diffusion phenomena.

Therefore, the analysis of the different impedance parameters, especially the CPE, indicates that SiPF provides slightly better corrosion resistance than SiF. Thus, the systems can be classified in terms of corrosion resistance as follows: SiPF > SiF > PCC-SiPF >> PCC-SiF >> PCC, AZ31B. Furthermore, there is correlation between the EIS and OCP results, both revealing self-healing effects as striking findings. Then, the complementary information of both techniques is able to confirm that the self-healing effect occurs not only in the barrier PEO layer but also due to the sealing of the outer PEO layer, especially for the SiPF system.

3.4. Coating characterization after immersion in 0.5 wt.% NaCl

In order to provide more insights into the corrosion performance of the coatings, further characterization was performed using optical images and SEM-EDS. Three immersion times were selected based on the opposing trends of the OCP for the PEO systems (Fig. 13): 12 h (when the OCP is still rising), 48 h (when the OCP is decreasing) and 168 h (when the OCP reaches steady state).

Table 8 presents optical images for all systems alongside their $|Z|_{0.01\ Hz}$ values at each time point. A circular shape, attributable to the O-ring of the electrochemical cell, is evident in most samples. From the start, the AZ31B magnesium alloy underwent severe corrosion, resulting in nearly complete coverage by corrosion products after 168 h. The PCC coating displays whitish corrosion products after 12 h, while dark spots—likely indicative of degradation—are observed on the PEO with precursor. However, the $|Z|_{0.01\ Hz}$ are still between 10^6 and 10^7 Ωcm^2. For the SiF and SiPF, aesthetic changes were noted at 168 h; specifically, SiF exhibited a darker surface than SiPF. Interestingly, this aesthetic variation in SiF does not correspond to a significant drop in $|Z|_{0.01\ Hz}$. Further corrosion testing using hydrogen evolution measurements over a period of 168 h confirmed the excellent corrosion resistance of the studied PEO coatings, with corrosion rates that were negligible compared to the bare AZ31B alloy (Figure S14).

Fig. 19 includes longitudinal and cross-sectional SEM images, providing an overview of the surface over time. Regardless of the PEO system used, the morphology is significantly altered after 168 h due to the appearance of cracks. This could be attributed to volume expansion caused by progressive hydration rather than the formation of corrosion products. In fact, no signs of pitting or undercoating corrosion were found in the cross-sectional images for the SiF and SiPF systems, even after 168 h of immersion (Figure S15). This hydration may explain the increase in OCP observed during the first 12 h of immersion for all PEO systems (Fig. 13), as it leads to the sealing or blocking of pores and cracks throughout the coating thickness. The pH in these regions can easily exceed 10.5, which stabilizes the formation of $Mg(OH)_2$ as passive

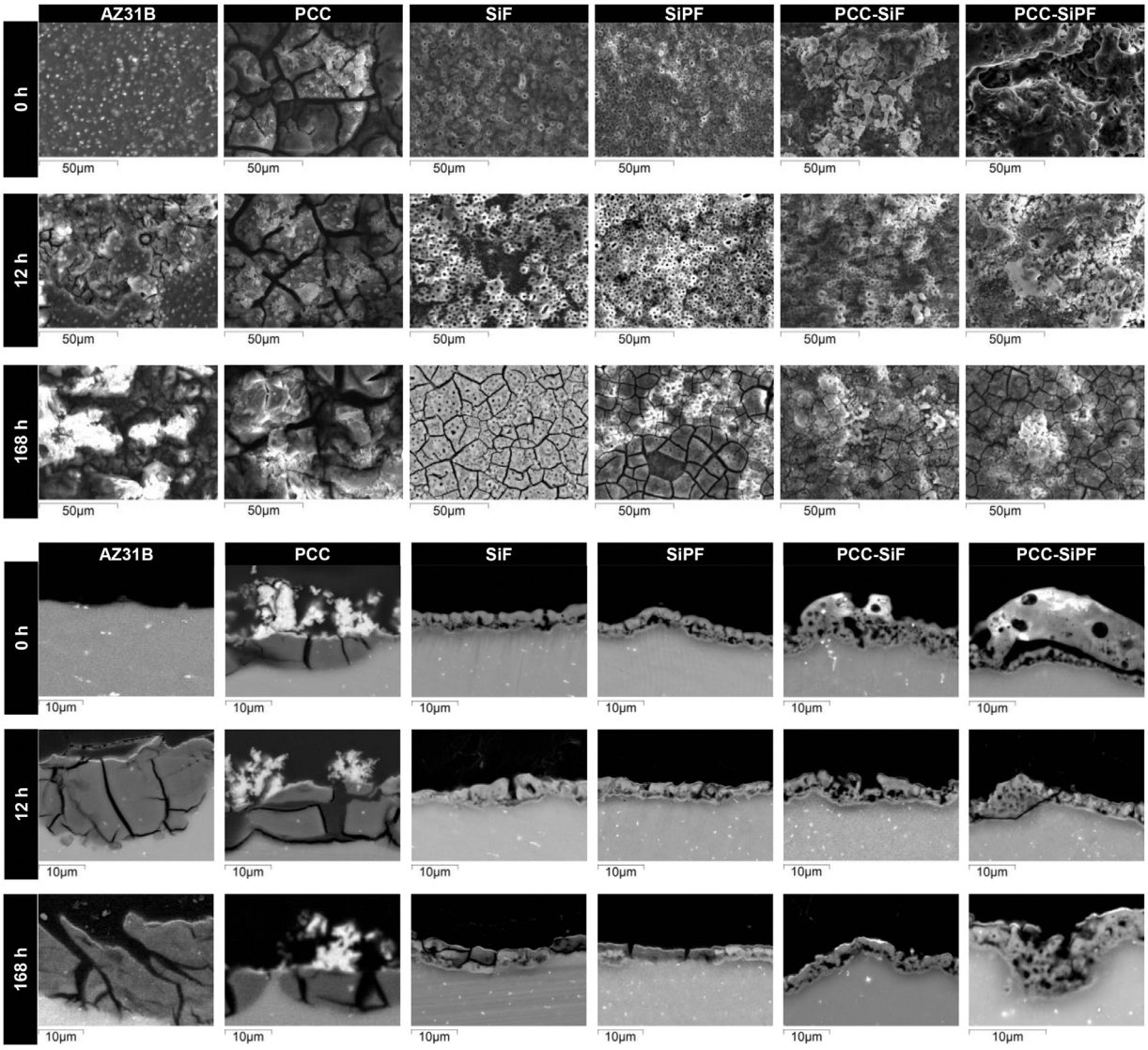

Fig. 19. Plan view BS SEM images (top) for samples immersed in 0.5 wt.% NaCl for 12 h and 168 h and cross-sectional BS SEM images (bottom) for samples immersed in 0.5 wt.% NaCl for 12 h and 168 h, compared with references (0 h).

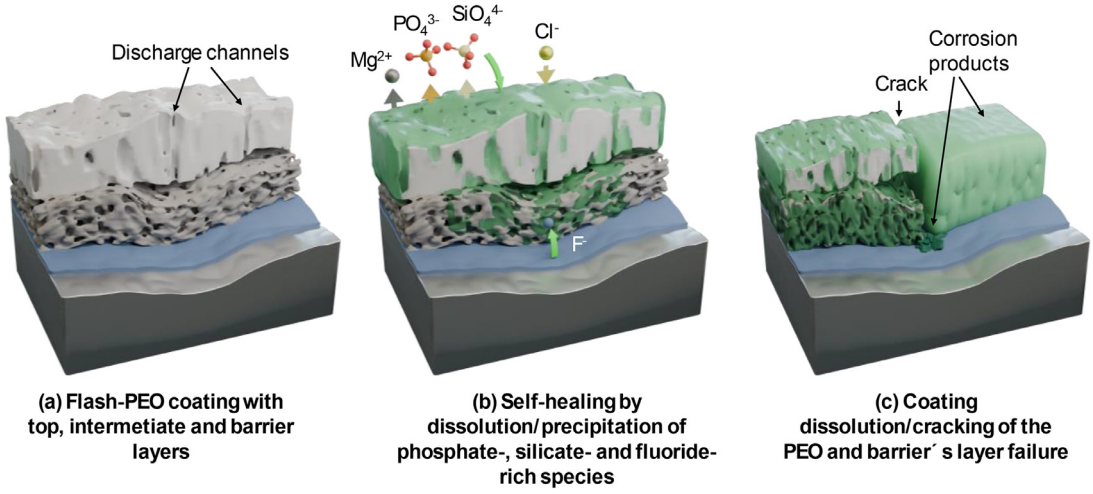

Fig. 20. Corrosion mechanism of the Flash-PEO coatings: (a) as received, (b) dissolution and precipitation of compounds, and (c) dissolution and cracking of the coating and barrier layer failure.

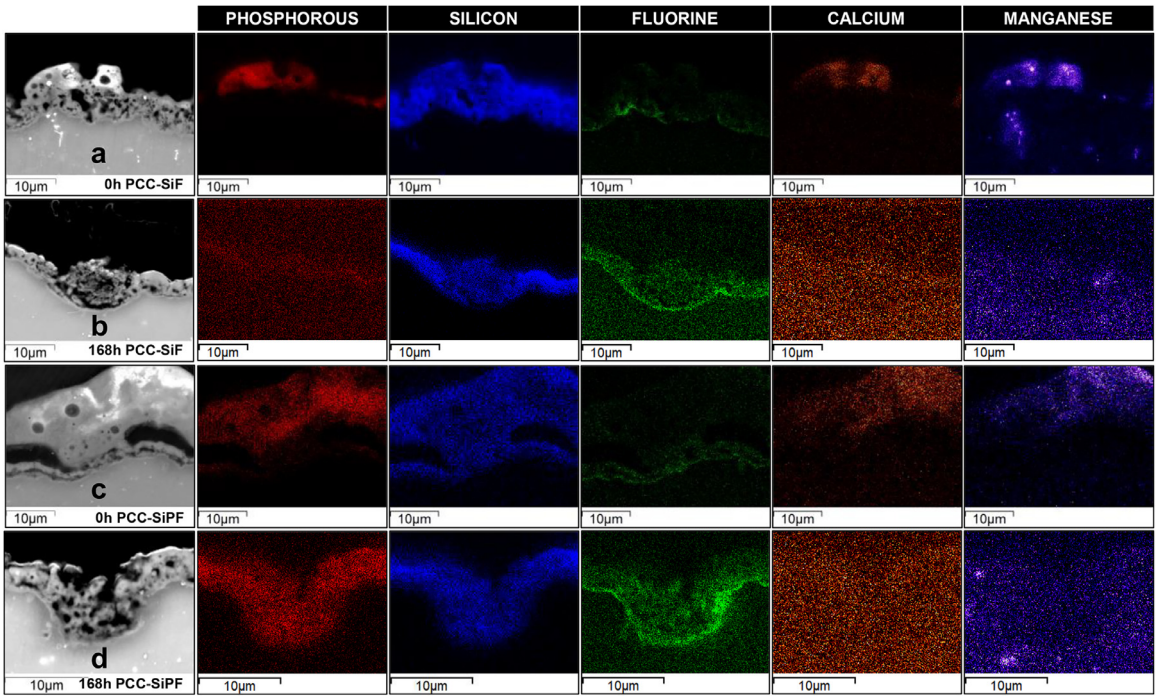

Fig. 21. EDS maps of P, Si, F, Ca and Mn of a) PCC-SiF, b) PCC-SiF after 168 h of immersion, c) PCC-SiPF, and b) PCC-SiPF after 168 h of immersion.

Table 8
Visual appearance of the samples by optical microscopy and average $|Z|_{0.01\ Hz}$ at 48 h and 168 h of immersion in 0.5 wt.% NaCl (area exposed equals to 1 cm^2).

Sample	12 h	48 h	$\|ZI_{0.01\ Hz}$ 48 h [Ωcm^2]	168 h	$\|ZI_{0.01\ Hz}$ 168 h [Ωcm^2]
PCC-SiPF		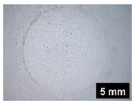	1.5×10^7	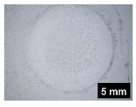	1.8×10^5
PCC-SiF			2.8×10^6		3.9×10^3
SiPF			1.9×10^7	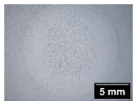	3.6×10^5
SiF	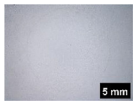	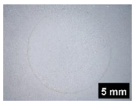	6.6×10^6	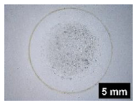	3.6×10^5
PCC	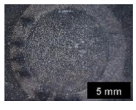	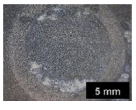	1.8×10^3	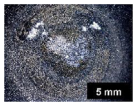	2.1×10^3
AZ31B Reference	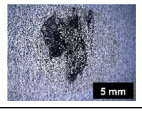	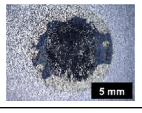	3.5×10^3	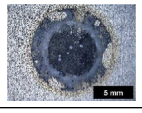	9.8×10^2

film [70]. Additionally, other compounds, such as silicates [71] and phosphates [72], might also contribute through a dissolution/precipitation mechanism, which has been depicted in Fig. 20.

The sealing of the pores appears less effective in the PCC-SiF system after 168 h, as indicated by the low $|Z|_{0.01\ Hz}$ values. In the PCC-SiPF system, although cross-sectional images suggest some degradation of the barrier layer after 168 h (consistent with its high CPE_{in} values, Table 7), the $|Z|_{0.01\ Hz}$ values still indicate a certain level of protection.

Cross-sectional elemental maps in Fig. 21 compare the structured coatings before and after 168 h of immersion in

0.5 wt.% NaCl. The most important findings are as follows: 1) the distribution of phosphorous and silicon along the coatings appears to be more uniform, suggesting self-healing effects; 2) fluorine spreads throughout the coating after immersion, rather than being primarily confined to the barrier layer; 3) manganese is mostly associated with the PCC precursor; and 4) calcium seems to leach out of the coating after immersion. The redistribution of fluorine could suggest degradation of the barrier layer, while the behaviour of calcium needs to be explored in more detail.

4. Conclusions

Silicate-fluoride and silicate-phosphate-fluoride Flash-PEO coatings, incorporating a phosphate conversion coating as a precursor, have been successfully obtained on AZ31B magnesium alloy. The PCC layer alters the typical discharge regime and, as a result, modifies the morphology of the structured coating, resulting in larger pores. TEM and SEM-EDS findings reveal that the discharges interact with PCC layer, which becomes integrated into the PEO coating, forming P-rich flakes that also contain Ca, Zn and Mn. TEM further reveals the presence of oxidized disks beneath the barrier layer and remnants of discharge channels, creating pathways to the substrate and making these areas prone to corrosion microcells. These areas may account for the metastable behaviour observed in the OCP values, especially when the precursor is present. After 168 h of immersion in 0.5 wt.% NaCl solution, the PCC-SiPF system demonstrated similar corrosion resistance comparable to the SiF and SiPF systems, thought EIS resistance and capacitance parameters indicate slightly better performance of the latter. This confirms that the incorporation of phosphates into the coating is beneficial from a corrosion point view, especially when sourced from the electrolyte. Despite the differences in coating performance, sealing of the pores and coating defects occurs during immersion, which explains the relatively high OCP values and the excellent performance of the studied coatings. Further studies of precursor-modified Flash-PEO coatings should aim at achieving uniformly distributed small pores to facilitate self-healing mechanisms.

Data availability statement

All data presented in this work will be made available through Docta Complutense repository. https://docta.ucm.es/handle/20.500.14352/16.

Declaration of competing interest

The authors declare that they have no known competing financial interests or personal relationships that could have appeared to influence the work reported in this paper.

CRediT authorship contribution statement

M.H. Guerra-Mutis: Writing – review & editing, Writing – original draft, Validation, Investigation, Formal analysis, Data curation. **J.M. Vega:** Writing – review & editing, Supervision, Methodology, Formal analysis, Conceptualization. **M.I. Barrena:** Writing – review & editing. **E. Matykina:** Writing – review & editing. **R. Arrabal:** Writing – review & editing, Supervision, Project administration, Methodology, Formal analysis, Conceptualization.

Acknowledgements

The authors gratefully acknowledge the support of the PID2021–124341OB-C22/AEI/10.13039/501100011033/FEDER, UE (MICIU). J.M. Vega also acknowledges the Grant RYC2021–034384-I funded by MICIU/AEI/10.13039/501100011033 and by "European Union NextGenerationEU/PRTR".

Supplementary materials

Supplementary material associated with this article can be found, in the online version, at doi:10.1016/j.jma.2025.01.007.

References

[1] M. Esmaily, et al., Prog Mater Sci 89 (2017) 92–193, doi:10.1016/j.pmatsci.2017.04.011.
[2] J. Song, et al., J Magnesium and Alloys 10 (4) (2022) 863–898, doi:10.1016/j.jma.2022.04.001.
[3] G. Song, A. Atrens, Adv Eng Mater 5 (12) (2003) 837–858, doi:10.1002/adem.200310405.
[4] Avedesian, M.M. and H.H. Baker. 1999.
[5] C.-y. Wu, J. Zhang, Transact Nonferrous Metals Soc China 21 (4) (2011) 892–902, doi:10.1016/S1003-6326(11)60799-1.
[6] H. Henry, N. Xueyuan, and M. Yueyu, Corrosion and Surface Treatment of Magnesium Alloys, in Magnesium Alloys, C. Frank, Editor. 2014, IntechOpen: Rijeka. pp. 67–108.
[7] X. Dong , in Handbook of Manufacturing Engineering and Technology, A.Y.C. Nee, Editor. 2015, Springer London pp. 3031–3054.
[8] F.E.-T. Heakal, and A.E. Elkholy, in Advances in Smart Coatings and Thin Films For Future Industrial and Biomedical Engineering Applications, A.S.H. Makhlouf and N.Y. Abu-Thabit, Editors. 2020, Elsevier. pp. 263–287.
[9] C. Vinoth Kumar, G. Rajyalakshmi, J. Kartha, J Bio- and Tribo-Corrosion 9 (2022) 13, doi:10.1007/s40735-022-00732-7.
[10] V.S. Saji, Advances in Corrosion Control of Magnesium and Its Alloys: Metal Matrix Composites and Protective Coatings, CRC Press, Boca Raton, 2023.
[11] T.M. Yue, K.J. Huang, Mater Trans 52 (4) (2011) 810–813, doi:10.2320/matertrans.M2010274.
[12] T. Wu, K. Zhang, Coatings 13 (2023) 1533, doi:10.3390/coatings13091533.
[13] R. Arrabal, M. Mohedano, E. Matykina, in: Encyclopedia of Materials: Metals and Alloys, Elsevier, 2021, pp. 87–112.
[14] A.S. Gnedenkov, et al., J Magnesium and Alloys 11 (10) (2023) 3688–3709, doi:10.1016/j.jma.2023.07.016.
[15] A.S. Gnedenkov, et al., J Magnesium and Alloys 12 (7) (2024) 2909–2936, doi:10.1016/j.jma.2024.07.004.
[16] X.B. Chen, N. Birbilis, T.B. Abbott, Corrosion 67 (3) (2011) 035005-1-035005-16, doi:10.5006/1.3563639.
[17] M. Kaseem, Y.G. Ko, Mater Lett 221 (2018) 196–200, doi:10.1016/j.matlet.2018.03.119.
[18] M.A. Khan, et al., J Magnesium and Alloys 12 (2) (2024) 586–607, doi:10.1016/j.jma.2023.12.004.

[19] W. Yang, et al., Appl Surf Sci 270 (2013) 519–525, doi:10.1016/j.apsusc.2013.01.073.
[20] B. Vaghefinazari, et al., Materials (Basel) 15 (2022) 8676, doi:10.3390/ma15238676.
[21] M.A. Hafeez, et al., J Coat Technol Res 17 (4) (2020) 827–849, doi:10.1007/s11998-020-00335-2.
[22] Y. Gao, A. Yerokhin, A. Matthews, Appl Surf Sci 316 (2014) 558–567, doi:10.1016/j.apsusc.2014.08.035.
[23] L. Pezzato, et al., J Appl Electrochem 44 (7) (2014) 867–879, doi:10.1007/s10800-014-0695-x.
[24] E. Wierzbicka, et al., Materials (Basel) 15 (2022) 8515, doi:10.3390/ma15238515.
[25] E. Wierzbicka, et al., Corros Sci 180 (2021) 109189, doi:10.1016/j.corsci.2020.109189.
[26] M.A. Iqbal, et al., Surface and Coatings Technol 476 (2024) 130186, doi:10.1016/j.surfcoat.2023.130186.
[27] Y. Xiong, et al., J Alloys Compd 822 (2020) 153707, doi:10.1016/j.jallcom.2020.153707.
[28] B. Zhu, et al., J Biomater Appl 36 (9) (2022) 1664–1675, doi:10.1177/08853282211046776.
[29] L. Rama Krishna, et al., J Alloys Compd 578 (2013) 355–361, doi:10.1016/j.jallcom.2013.06.036.
[30] J. Martin, et al., Surface and Coatings Technol 392 (2020) 125756, doi:10.1016/j.surfcoat.2020.125756.
[31] S. Thunaipragasam, et al., Journal of Nanomaterials 2023 (1) (2023) 7267093, doi:10.1155/2023/7267093.
[32] A. Madhan Kumar, et al., Mater Chem Phys 149-150 (2015) 480–486, doi:10.1016/j.matchemphys.2014.10.049.
[33] J. Dou, et al., Physical Chem Chemical Physics 19 (23) (2017) 15110–15119, doi:10.1039/C7CP02672B.
[34] L. Sun, et al., Surface and Coatings Technol 390 (2020) 125661, doi:10.1016/j.surfcoat.2020.125661.
[35] S. Hariprasad, et al., J Alloys Compd 722 (2017) 698–715, doi:10.1016/j.jallcom.2017.06.119.
[36] H. Zhu, et al., Metals and Materials Int 27 (10) (2021) 3975–3982, doi:10.1007/s12540-020-00656-2.
[37] K. Qian, et al., Corros Sci 226 (2024) 111674, doi:10.1016/j.corsci.2023.111674.
[38] E. Wierzbicka, et al., Metals (Basel) 11 (2021) 337, doi:10.3390/met11020337.
[39] M. Klinger, A. Jager, J Appl Crystallogr 48 (6) (2015) 2012–2018, doi:10.1107/S1600576715017252.
[40] ISO (2017). https://www.iso.org/home.html.
[41] L. Wang, et al., Mater Res Express 7 (1) (2020) 016412, doi:10.1088/2053-1591/ab60a7.
[42] E. Lopez-Martinez, et al., J Materials Res Technol 31 (2024) 1786–1796, doi:10.1016/j.jmrt.2024.06.171.
[43] L. Moreno, et al., J Magnesium and Alloys 10 (8) (2022) 2220–2237, doi:10.1016/j.jma.2021.12.011.
[44] C.E. Barchiche, D. Veys-Renaux, E. Rocca, Surface and Coatings Technol 205 (17) (2011) 4243–4248, doi:10.1016/j.surfcoat.2011.03.019.
[45] Z. Li, et al., Corros Sci 157 (2019) 295–304, doi:10.1016/j.corsci.2019.06.005.
[46] J. Yang, et al., Corros Sci 140 (2018) 99–110, doi:10.1016/j.corsci.2018.06.014.
[47] T.W. Clyne, S.C. Troughton, Int Mater Rev 64 (3) (2019) 127–162, doi:10.1080/09506608.2018.1466492.
[48] L. Wang, et al., J Alloys Compd 480 (2) (2009) 469–474, doi:10.1016/j.jallcom.2009.01.102.
[49] C. Blawert, et al., Surface and Coatings Technol 213 (2012) 48–58, doi:10.1016/j.surfcoat.2012.10.013.
[50] X. Lu, et al., Surface and Coatings Technol 307 (2016) 1165–1182, doi:10.1016/j.surfcoat.2016.08.055.
[51] V. Belevantsev, et al., in: Micro-plasma Electrochemical Processes, 34, Protection of Metals, 1998, pp. 416–430. https://scholar.google.com.
[52] J. Martin, et al., Mater Des 178 (2019) 107859, doi:10.1016/j.matdes.2019.107859.
[53] N. Nashrah, S.H. Baek, Y.G. Ko, J Magnesium and Alloys 10 (8) (2022) 2185–2192, doi:10.1016/j.jma.2021.06.009.
[54] S. Ikonopisov, Electrochim. Acta 22 (10) (1977) 1077–1082, doi:10.1016/0013-4686(77)80042-X.
[55] P. Bruggeman, C. Leys, J Phys D Appl Phys 42 (5) (2009) 053001, doi:10.1088/0022-3727/42/5/053001.
[56] R.O. Hussein, et al., J Phys D Appl Phys 43 (10) (2010) 105203, doi:10.1088/0022-3727/43/10/105203.
[57] Y. Takahashi, J Electrostat 6 (1) (1979) 1–13, doi:10.1016/0304-3886(79)90020-2.
[58] W. An, K. Baumung, H. Bluhm, J Appl Phys 101 (5) (2007) 053302, doi:10.1063/1.2437675.
[59] M. Ngo Huu, et al., Appl Sci 10 (10) (2020) 3569, doi:10.3390/app10103569.
[60] R. Nates, Universal J Mechanical Engineering 3 (5) (2015) 185–201, doi:10.13189/ujme.2015.030504.
[61] ASTM Standard D7334 − 08 (Reapproved 2022) . (2022). https://www.astm.org.
[62] A. Rudawska, et al., Appl Sci 13 (2023) 10059, doi:10.3390/app131810059.
[63] A. Hunt, Lect. Notes Phys 674 (2005).
[64] A. Castellanos, et al., Surface and Coatings Technol 278 (2015) 99–107, doi:10.1016/j.surfcoat.2015.07.017.
[65] S. Feliu, Metals (Basel) 10 (2020) 775, doi:10.3390/met10060775.
[66] T.S. Lim, H.S. Ryu, S.-H. Hong, Corros Sci 62 (2012) 104–111, doi:10.1016/j.corsci.2012.04.043.
[67] A.S. Gnedenkov, et al., Materials (Basel) 16 (2023) 2215, doi:10.3390/ma16062215.
[68] A.C. Lazanas, M.I. Prodromidis, ACS Measurement Science Au 3 (3) (2023) 162–193, doi:10.1021/acsmeasuresciau.2c00070.
[69] Lingjie, L., F. Pan, and L. Jinglei, Environmental Friendly Corrosion Inhibitors for Magnesium Alloys, in Magnesium Alloys - Corrosion and Surface Treatments, F. Czerwinski, Editor. 2011, p. 47–64.
[70] X. Lu, et al., Surface and Coatings Technol 269 (2015) 155–169, doi:10.1016/j.surfcoat.2014.11.027.
[71] B.-l. Lin, J.-t. Lu, Trans Nonferrous Metals Soc China 24 (8) (2014) 2723–2728, doi:10.1016/S1003-6326(14)63403-8.
[72] X. Xue, et al., J Alloys Compd 960 (2023) 170710, doi:10.1016/j.jallcom.2023.170710.